Diagnosing Convective Dependencies on Near-Storm Environments Using Ensemble Sensitivity Analyses

CHRISTOPHER A. KERR

School of Meteorology, and Cooperative Institute for Mesoscale Meteorological Studies, University of Oklahoma, and NOAA/National Severe Storms Laboratory, Norman, Oklahoma

DAVID J. STENSRUD

Department of Meteorology and Atmospheric Science, The Pennsylvania State University, University Park, Pennsylvania

XUGUANG WANG

School of Meteorology, University of Oklahoma, Norman, Oklahoma

ABSTRACT

Convection intensity and longevity is highly dependent on the surrounding environment. Ensemble sensitivity analysis (ESA), which quantitatively and qualitatively interprets impacts of initial conditions on forecasts, is applied to very short-term (1–2 h) convective-scale forecasts for three cases during the Mesoscale Predictability Experiment (MPEX) in 2013. The ESA technique reveals several dependencies of individual convective storm evolution on their nearby environments. The three MPEX cases are simulated using a previously verified 36-member convection-allowing model ($\Delta x = 3$ km) ensemble created via the Weather Research and Forecasting (WRF) Model. Radar and other conventional observations are assimilated using an ensemble adjustment Kalman filter. The three cases include a mesoscale convective system (MCS) and both nontornadic and tornadic supercells. Of the many ESAs applied in this study, one of the most notable is the positive sensitivity of supercell updraft helicity to increases in both storm inflow region deep and shallow vertical wind shear. This result suggests that larger values of vertical wind shear within the storm inflow yield higher values of storm updraft helicity. Results further show that the supercell storms quickly enhance the environmental vertical wind shear within the storm inflow region. Application of ESA shows that these storm-induced perturbations then affect further storm evolution, suggesting the presence of storm–environment feedback cycles where perturbations affect future mesocyclone strength. Overall, ESA can provide insight into convection dependencies on the near-storm environment.

1. Introduction

Convection-allowing models (CAMs) can improve predictions of the organization and evolution of convection (e.g., Kain et al. 2006, 2008; Clark et al. 2010a,b). Reliable forecasts of deep convection are needed to improve warnings for associated high-impact meteorological phenomena (e.g., damaging winds, flash flooding, hail, tornadoes; Stensrud et al. 2009, 2013). The practical predictability of such events is largely dependent on having accurate initial conditions and small model error (Zhang et al. 2007;

Cintineo and Stensrud 2013; Johnson et al. 2014; Johnson and Wang 2016). Results from Cintineo and Stensrud (2013) suggest that near-storm environments must be well represented by the models to ensure reasonable forecast accuracy. Thus, impacts of long-lived convection on the environment (i.e., upscale feedbacks) must be well depicted in model forecasts. In this study, the dependencies of convection evolution on the surrounding environment are evaluated using an ensemble sensitivity analysis technique (Torn and Hakim 2008).

Upscale feedbacks on the surrounding environment by convective storms are described in many past studies (Maddox 1980; Fritsch and Maddox 1981a,b; Brooks et al. 1994). Most studies use numerical models to

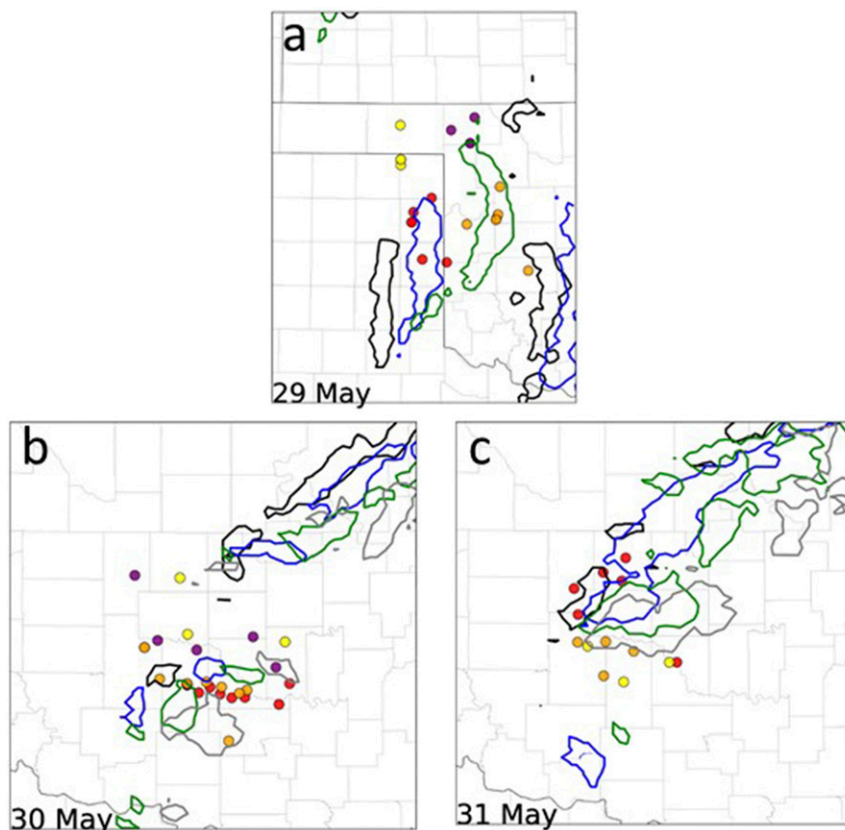*Corresponding author*: Christopher A. Kerr, christopher.kerr@noaa.gov

FIG. 1. Hourly observed reflectivity 30-dBZ contours for (a) 2100 UTC (black), 2200 UTC (blue), and 2300 UTC (green) 29 May; (b) 1900 UTC (black), 2000 UTC (blue), 2100 UTC (green), and 2200 UTC (gray) 30 May; (c) 2200 UTC (black), 2300 UTC (blue) 31 May and 0000 UTC (green), 0100 UTC (gray) 1 Jun. Circles denote upsondes released during MPEX by color designated team [adapted from Kerr et al. (2017)].

present these impacts (e.g., Maddox 1980; Fritsch and Maddox 1981b; Brooks et al. 1994; Stensrud 1996; Stensrud and Anderson 2001), while some studies use observations (e.g., Fritsch and Maddox 1981a; Parker 2014). In the storm-relative local mesoscale environment, Brooks et al. (1994) note the enhancement of convective available potential energy (CAPE) and storm-relative helicity (SRH) within the storm's inflow region. Stensrud (1996) shows low-level inflow wind speeds increase with persistent convection. This study uses CAMs to further describe the impacts convection has on the environmental vertical wind shear and low-level storm inflow. Convective perturbations are described in terms of distance from storms of interest and temporally, while ensemble sensitivity analysis is utilized to reveal the significance of storm-induced vertical wind shear and inflow changes on further convection evolution.

This study focuses on specific convective events within a 3-day period from 29 to 31 May 2013 where the near-storm environments were verified against Mesoscale

Predictability Experiment (MPEX; Weisman et al. 2015; Trapp et al. 2016; Coniglio et al. 2016; Hitchcock et al. 2016) upsondes (Kerr et al. 2017). On 29 May a linear system is featured that grows into a mesoscale convective system (MCS), beginning in the Texas Panhandle and moving into western Oklahoma (Fig. 1a). This case has substantial cold pool growth that drives the convection evolution. A non-tornadic supercell in central Oklahoma on 30 May (Fig. 1b) provides the opportunity to analyze the convection perturbations to the storm inflow regions as described in previous studies (Brooks et al. 1994; Stensrud 1996). Last, the simulation of a large tornadic supercell from 31 May (Fig. 1c) is explored. This supercell produced a large, violent tornado west of Oklahoma City (Bluestein et al. 2015).

The next section describes the experiment design and data assimilation techniques used to properly create the model state. Section 3 presents the results of ensemble sensitivity analysis applied to the convective-scale including convection–environment feedbacks, and a discussion is presented in section 4.
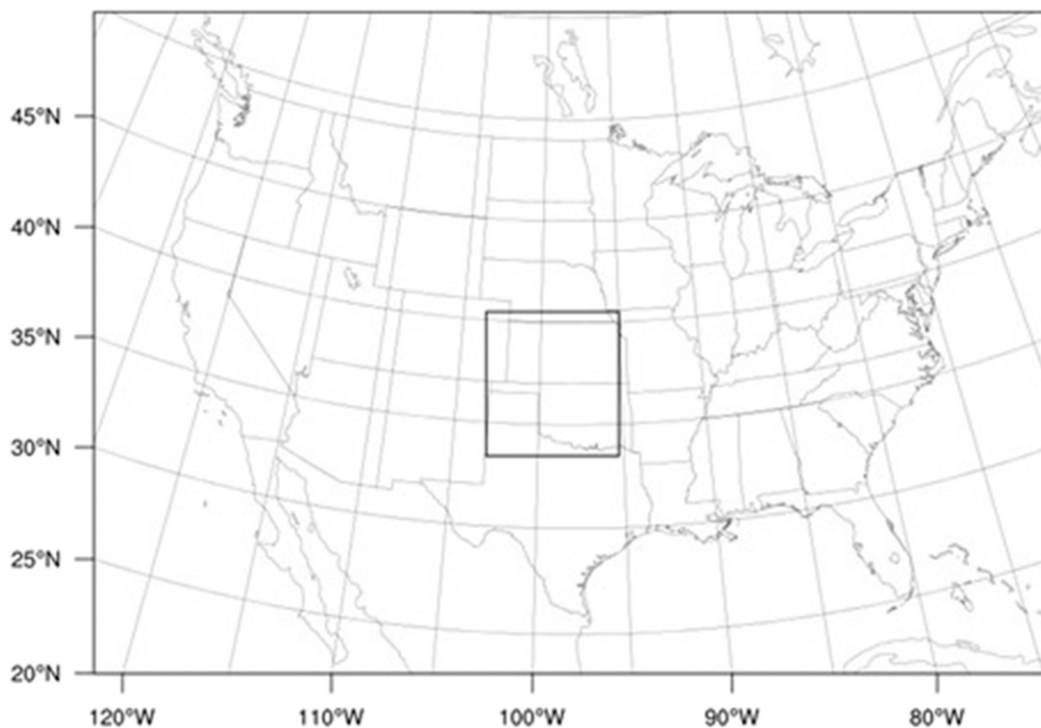
FIG. 2. Outer model domain (CONUS; 15-km grid spacing) and nested, convection-resolving domain (3-km grid spacing) that includes KS, OK, and the TX Panhandle [adapted from Kerr et al. (2017)].

2. Experimental design

Three case studies are simulated using an ensemble design known as the National Severe Storms Laboratory (NSSL) Experimental Warn-on-Forecast System for ensembles (NEWS-e) as described in Wheatley et al. (2015), Jones et al. (2016), and Kerr et al. (2017). This setup uses the Advanced Research version of WRF (WRF-ARW), version 3.4.1 (Skamarock et al. 2008), where a one-way nested domain is placed over portions of Texas, Oklahoma, and Kansas to encompass all events of interest in this 3-day sequence (Fig. 2). The inner, storm-scale domain has a horizontal grid spacing of 3 km whereas the outer, mesoscale domain (CONUS) has a grid spacing of 15 km. Both domains have 51 vertical layers from the surface to 10 hPa, and the low-level storm inflow layer has a 300–500-m vertical spacing. The ensemble is initialized at 0000 UTC each day using a downscaled 18-member Global Ensemble Forecast System (GEFS). The outer domain boundary conditions are created using the GEFS, while the outer domain provides the boundary conditions for the inner domain.

Ensemble members are created using the methodology outlined by Wheatley et al. (2015) where a combination of 18 GEFS members and 18 physics combinations of planetary boundary layer (PBL), longwave and shortwave radiation, and convective (outer domain only) parameterization schemes yield 36 ensemble members (Table 1). All ensemble members utilize the Thompson et al. (2008) microphysics scheme. Members 1–18 are initialized with the same numerical GEFS member and are run with the same numerical physics combination from Table 1. Members 19–36 are initialized with the same 18 GEFS members in descending order (member 19 with GEFS member 18, member 20 with GEFS member 17, etc.) while running the physics combinations in ascending order (member 19 with combination 1, member 20 with combination 2, etc.) Given there are 18 unique initial conditions at 0000 UTC (given only 18 GEFS members), the model is integrated 1 h forward to create 36 unique initial conditions. Further details of this approach can be found in Wheatley et al. (2015), Jones et al. (2016), and Kerr et al. (2017).

a. Mesoscale data assimilation

At 0100 UTC, mesoscale data assimilation begins with hourly update cycles. Temperature, dewpoint, pressure, and zonal and meridional wind component observations are provided by the NOAA Meteorological Assimilation Data Ingest System (MADIS) and assimilated using an ensemble adjustment Kalman filter (EAKF; Anderson 2001) available via the Data Assimilation Research Testbed (DART;

TABLE 1. Physics options applied to 18 GEFS members. This set of physics options also is applied to these same 18 GEFS members in reverse order to create members 19–36 (e.g., member 19 is initialized with GEFS member 18 but has physics option 1 applied). The Thompson microphysics and RAP land surface parameterization is applied to all members. PBL schemes include the Yonsei University (YSU), Mellor–Yamada–Janjić (MYJ), and Mellor–Yamada–Nakanishi–Niino (MYNN) schemes. Shortwave (SW) and longwave (LW) radiation schemes include the Dudhia shortwave scheme, Rapid Radiative Transfer Model (RRTM) shortwave scheme, and the Rapid Radiative Transfer Model for GCMs (RRTMG) shortwave and longwave schemes [adapted from Wheatley et al. (2015) and Kerr et al. (2017)].

Member	PBL	SW radiation	LW radiation	Cumulus
1	YSU	Dudhia	RRTM	Kain–Fritsch
2	YSU	RRTMG	RRTMG	Kain–Fritsch
3	MYJ	Dudhia	RRTM	Kain–Fritsch
4	MYJ	RRTMG	RRTMG	Kain–Fritsch
5	MYNN	Dudhia	RRTM	Kain–Fritsch
6	MYNN	RRTMG	RRTMG	Kain–Fritsch
7	YSU	Dudhia	RRTM	Grell
8	YSU	RRTMG	RRTMG	Grell
9	MYJ	Dudhia	RRTM	Grell
10	MYJ	RRTMG	RRTMG	Grell
11	MYNN	Dudhia	RRTM	Grell
12	MYNN	RRTMG	RRTMG	Grell
13	YSU	Dudhia	RRTM	Tiedtke
14	YSU	RRTMG	RRTMG	Tiedtke
15	MYJ	Dudhia	RRTM	Tiedtke
16	MYJ	RRTMG	RRTMG	Tiedtke
17	MYNN	Dudhia	RRTM	Tiedtke
18	MYNN	RRTMG	RRTMG	Tiedtke

Anderson et al. 2009). Observations include METAR and marine surface stations, the Aircraft Communications Addressing and Reporting System (ACARS), rawinsondes, and data from the MADIS and Oklahoma Mesonets.

The Gaspari and Cohn (1999) Gaussian-like localization function is applied to all assimilated observations. Nonmesonet mesoscale observations have a horizontal localization cutoff of approximately 458 km with a vertical localization cutoff of 8 km [as in Wheatley et al. (2012, 2015)]. The horizontal localization of mesonet observations is approximately 60 km [as in Sobash and Stensrud (2015), Wheatley et al. (2015), and Jones et al. (2016)]. Spatial and temporal prior adaptive inflation is used to maintain ensemble spread (Anderson 2007).

b. Storm-scale data assimilation

Storm-scale data assimilation begins at a time based on each day's convective event (Table 2). Radar data (level II radar reflectivity and radial velocity; radars listed in Table 2) are assimilated every 15 min with MADIS mesonet, Oklahoma Mesonet, and conventional rawinsonde observations. Radar observations have an 18-km horizontal localization cutoff and 6-km

vertical cutoff (Yussouf et al. 2013; Wheatley et al. 2014, 2015; Jones et al. 2016). Surface and conventional rawinsonde observations have the identical localization specifications as used in mesoscale data assimilation. The frequent storm-scale assimilation only updates the inner domain while the parent domain serves as lateral boundary conditions without data assimilation updates. Radar reflectivity observations less than 10 dBZ are set to 0 dBZ and considered clear-air reflectivity observations. Radial velocity observations are only included in the assimilation if they are collocated with radar reflectivity observations exceeding or equal to 20 dBZ.

Following the quality control of radar observations, these data are objectively analyzed to a 6-km Cartesian grid (Cressman 1959) by the Observation Processing and Wind Synthesis (OPAWS; Majcen et al. 2008) software (Wheatley et al. 2015; Jones et al. 2016). Radar observations obtained within a 15-min window centered on the analysis time are assimilated; observation errors of 5 dBZ for radar reflectivity and 3 m s^{-1} for radial velocity are assumed uniform and are held constant (Dowell et al. 2004; Aksoy et al. 2009; Yussouf et al. 2013; Wheatley et al. 2015; Jones et al. 2016). Convection spinup is aided by the additive noise technique developed by Dowell and Wicker (2009). Temperature, dewpoint, and horizontal wind field random perturbations are added to each member at grid points where the reflectivity innovations are >10 dBZ and reflectivity observations are >25 dBZ (Sobash and Wicker 2015). The storm-scale data assimilation cycling continues until the observed storms decay. Ensemble analyses are available every 15 min, and a time during the mature phase of each storm is chosen to provide the initial conditions for a 1- to 2-h ensemble forecast that is needed for the ensemble sensitivity analysis described in section 2c.

c. Ensemble sensitivity analysis

Ensemble sensitivity analysis (ESA) is a technique that uses a group of ensemble forecasts to reveal dependencies of forecast metrics on model variables (same or different) at an earlier time, including the model initial conditions (Ancell and Hakim 2007; Hakim and Torn 2008; Torn and Hakim 2008). This method is a simple linear regression derived from the response of a given scalar forecast metric to an initial condition variable at a specified grid point. The sensitivity is defined by

$$\frac{\partial J}{\partial x} = \frac{\text{cov}(J, x)}{\text{var}(x)},$$

where J is a scalar forecast metric, x is an initial condition variable at a grid point, and cov is covariance and

TABLE 2. Description of the convective events each day. The start times of radar data assimilation are listed with the corresponding radars that collected the data including Dodge City, KS (KDDC); Amarillo, TX (KAMA); Vance Air Force Base, OK (KVNX); Oklahoma City, OK (KTLX); and Frederick, OK (KFDR).

Date	Event	Radars	Start time
29 May	Texas Panhandle; western Oklahoma bow echo and bookend vortex	KAMA, KFDR, KDDC, KVNX	1700 UTC
30 May	Central Oklahoma nontornadic supercell	KTLX, KFDR	1700 UTC
31 May	Central Oklahoma tornadic supercell	KTLX, KFDR, KVNX	2100 UTC

var is variance of the given variables, respectively. It should be noted that sensitivity magnitudes increase if initial condition ensemble variance decreases. This caveat reinforces the need for the ensemble to not be underdispersive. Wheatley et al. (2015) present the dispersiveness of this ensemble.

ESA has recently been applied on the mesoscale to examine sensitivities in convection forecasts (Bednarczyk and Ancell 2015; Torn and Romine 2015; Weisman et al. 2015; Hill et al. 2016; Romine et al. 2016; Berman et al. 2017; Torn et al. 2017). In these studies, ESA is applied to convection-related variables, such as reflectivity, vertical velocity, and precipitation, within designated response regions. For example, Bednarczyk and Ancell (2015) and Hill et al. (2016) show convection to be sensitive to upstream, synoptic-scale features in both the upper and lower troposphere. Torn and Romine (2015), Weisman et al. (2015), and Romine et al. (2016) use ESA on MPEX cases where dropsonde observations were targeted in regions of high sensitivity. Results from Romine et al. (2016) suggest that targeted observations of upstream features helps improve convection forecasts in the 12–24-h range.

This study instead applies ESA to short-term (1–2 h) forecasts of a convective system on 29 May and to individual supercell thunderstorms on 30 and 31 May 2013. The model error associated with this multiphysics ensemble does not interfere with the validity of the results presented, as the initial condition variability dominates on these time scales. Multiple scatterplot examples show that forecast–initial condition relationships qualitatively hold for this ensemble's three PBL schemes (Fig. 3). Although the regression slopes differ among PBL schemes, slope signs are consistent and generally agree with the entire ensemble regression slope even with increased sampling error (12 members per scheme). These four examples are averages of 50 environment (nonprecipitating) grid points in close proximity of one another (within a 50-km radius). Kerr et al. (2017) show that model error arising from varying radiation schemes is less influential in this ensemble. The sensitivity of storm-related forecast metrics, including storm-averaged reflectivity, rainfall, and updraft helicity, to environmental initial condition variables,

including moisture and vertical wind shear, is investigated. Updraft helicity (UH) is the product of updraft velocity and vorticity defined over specific vertical layers (Kain et al. 2008), so when UH is calculated over the 2–5-km layer it is used to identify midlevel mesocyclones in model output, a characteristic of supercell storms. When UH is calculated over the 0–1-km layer, it is a measure of low-level mesocyclone intensity.

To help counteract potential ensemble sampling errors, a one-sample t test is applied to determine if linear sensitivities are statistically significant. The one-sample t test is applied to the 36-sample distribution regression slope coefficient estimate using a 95% confidence interval (Wilks 2011, section 7.2.5). If this requirement is met, then the null hypothesis that changes to an initial condition do not affect a forecast metric can be rejected. When a relationship between an initial condition variable and forecast metric is highly nonlinear, the sensitivity does not pass the significance test since the standard error–slope ratio is too large. In this study, sensitivity values are outlined where the null hypothesis is not rejected. However, the physical phenomena and spatial scales in this study are subject to nonlinear relationships, and many sensitivities that do not pass the statistical significance test are still physically meaningful.

Environmental features that affect convection evolution on the time scale of 1–2 h are generally in close proximity to convective storms (estimated using an advective time scale to be 100 km via an idealized supercell simulation, not shown). A sensitivity radius, equal to the advective time scale, is used and placed on the center the main updraft of the supercells in both cases studied. Values of sensitivity are set to zero beyond the sensitivity radius as spurious sensitivities can arise because of ensemble sampling error, a common issue in ensemble data assimilation and forecasting (e.g., Wheatley et al. 2015; Jones et al. 2016; Kerr et al. 2017). A sensitivity radius is not applied to the 29 May case given the size of the convective system relative to the display window for this case.

d. Convective perturbations

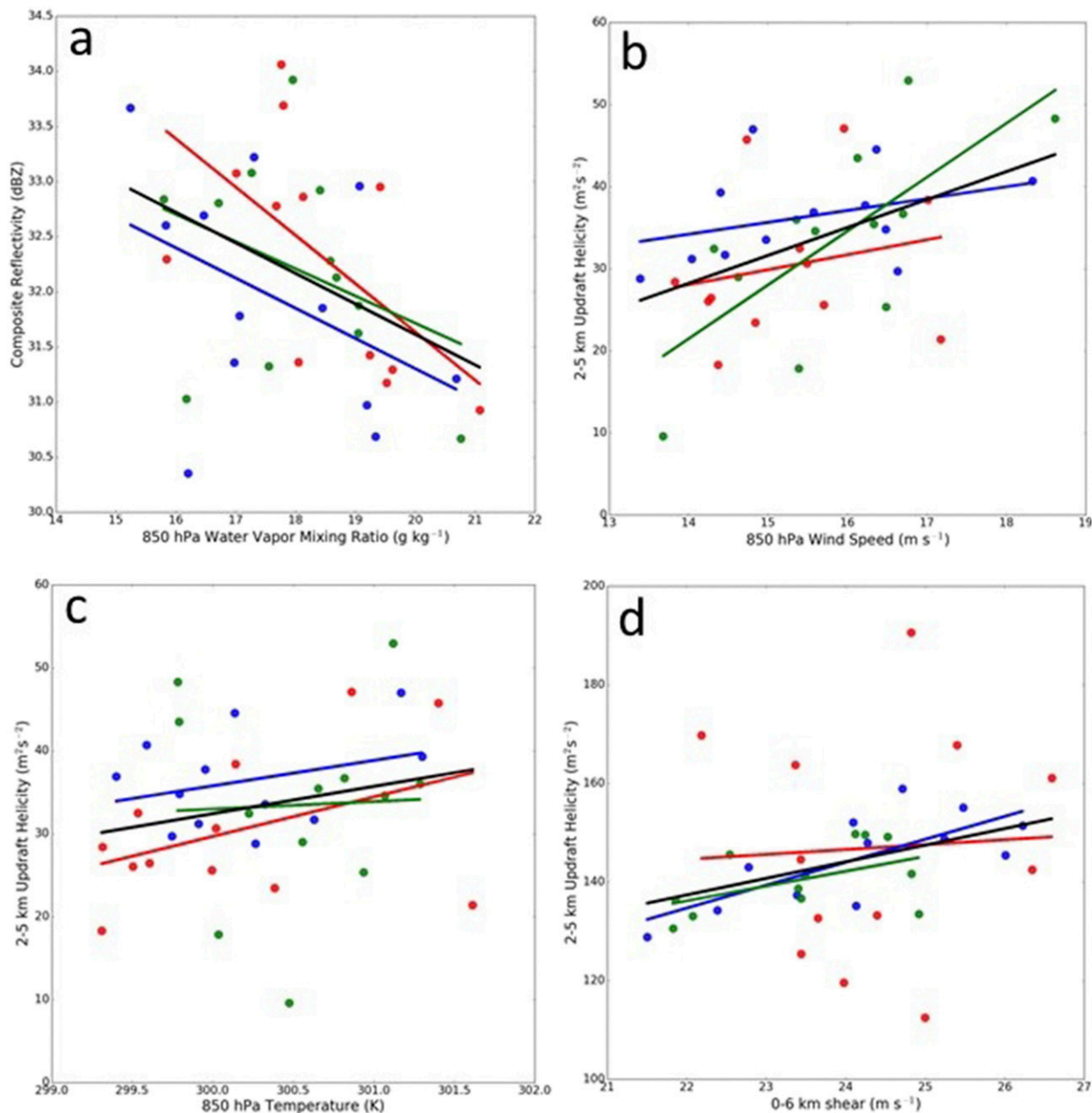Convective environments are known to be highly inhomogeneous over small spatial scales (Cortinas and

FIG. 3. Regression slopes of forecast metrics and inflow initial conditions averaged over 50 grid points. Color designates member PBL scheme [YSU (red), MYJ (blue), MYNN (green), all (black)] for (a) 29 May composite reflectivity and 850-hPa water vapor mixing ratio, (b) 30 May 2–5-km updraft helicity and 850-hPa wind speed, (c) 30 May 2–5-km updraft helicity and 850-hPa temperature, and (d) 31 May 2–5-km updraft helicity and 0–6-km vertical wind shear.

Stensrud 1995; Wagner et al. 2008; Kerr et al. 2017). Therefore, the environment can drastically change over a time period spanning a few hours even without the presence of convection. To discern whether short-term changes in the environment are convectively induced, a method is developed using the outer, mesoscale domain where convection is parameterized. In these case studies, parameterized convection on the outer domain does not

activate in the regions of targeted convection, such that the effects of shallow and deep convection are only seen in the model output on the inner domain (Figs. 4a,b).

The outer domain model state is linearly interpolated in the horizontal to the inner domain $\Delta x = 3$ km grid. The temporal changes in the fields on the downscaled outer domain are assumed to represent the evolution of the environment without convection. For the inner
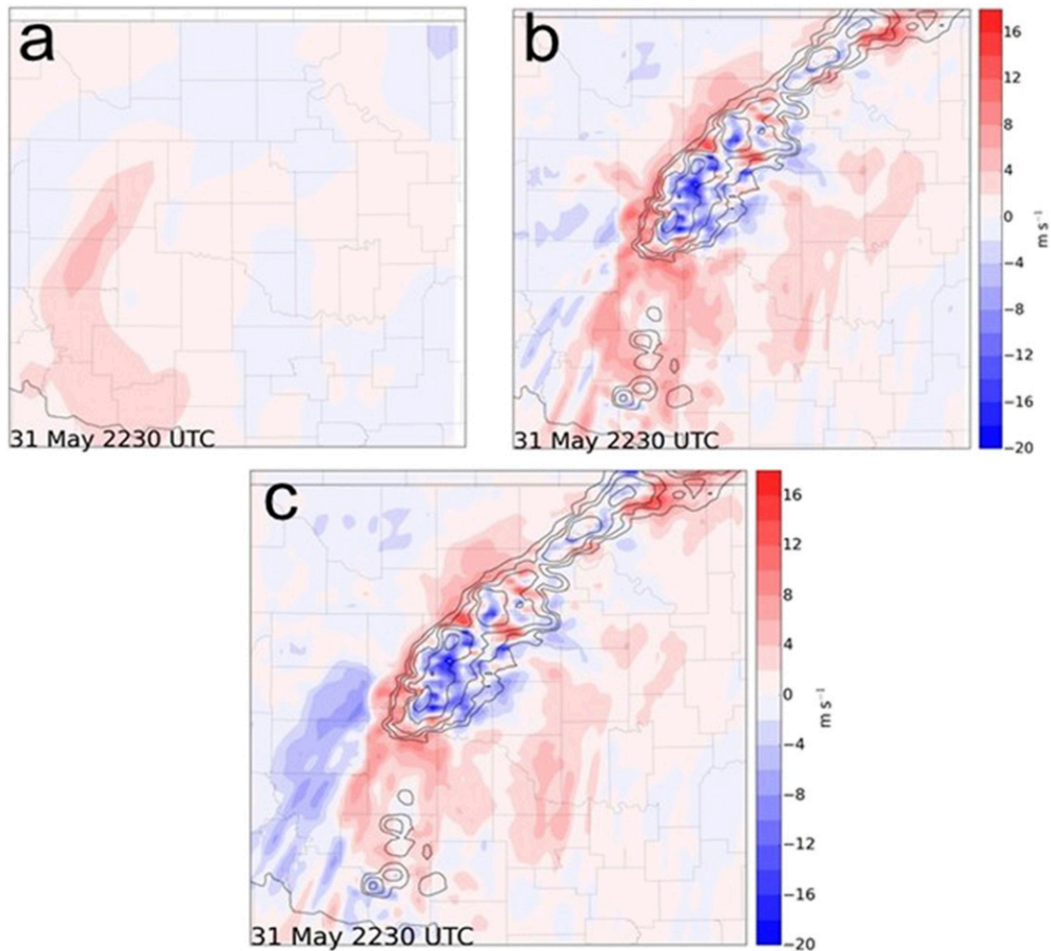
FIG. 4. The 1-h changes in ensemble mean analysis 0–6-km vertical wind shear from 2130 to 2230 UTC 31 May 2013 (filled) and low-level reflectivity analysis (black contours): (a) outer mesoscale domain, (b) inner storm-scale domain, and (c) difference between outer and inner domains, revealing changes induced by convection.

domain, the temporal changes represent the total change in the model state over a designated time period, including convectively induced changes as well as other environmental changes. To quantitatively determine the environmental features that are a result of convection, the temporal difference in the downscaled outer domain is subtracted from the temporal difference of the inner, convection-allowing domain over a specified time period (30 min, 1 h, etc.) that is the same for both domains. This difference quantifies how the mesoscale environment has been altered by nearby convection, as the environmental changes on the outer domain are assumed to be nonconvective perturbations. Results from 31 May 2013 show that the storm increases the 0–6-km vertical wind shear in only 1 h, but particularly in the inflow regions to the south and east of the target supercell (Fig. 4c). The differences between the outer and inner domain 0–6-km vertical wind shear changes are a factor

of 4 in maximum magnitude. Although this method is imperfect given interpolation and model errors, the method crudely removes qualitative temporal environmental changes not related to convection for the purposes of this study.

3. Results

For the three convective events selected (29 May, 30 May, 31 May), 3-km CAM ensemble forecasts of 1–2 h in length are created for each event. As described above, these forecasts are initialized from ensemble analyses several hours after convection initiation when the convection is well depicted by the ensemble members. This reduces the impacts of model error arising from the multiphysics ensemble, which are more prominent during convection initiation (e.g., Hohenegger et al. 2006; Leoncini et al. 2010; Keil et al. 2014;

TABLE 3. List of scalar forecast metrics (J) and initial condition variables (x) for which ESA is applied on each day.

Day	Forecast metric J	Initial condition x
29 May	Storm-averaged composite radar reflectivity	850-hPa wind speed
		850-hPa temperature
		850-hPa water vapor mixing ratio
30 May	Storm-averaged composite radar reflectivity	850-hPa water vapor mixing ratio
	Storm-averaged 2–5-km UH	0–6-km wind shear
		850-hPa temperature
31 May	Storm-averaged composite radar reflectivity	850-hPa water vapor mixing ratio
	Storm-averaged accumulated rainfall	850-hPa water vapor mixing ratio
	Storm-averaged 2–5-km UH	0–6-km wind shear
	Storm-averaged 0–1-km UH	0–1-km wind shear

Flack et al. 2018). As shown by Kerr et al. (2017), these ensemble analyses accurately depict ongoing convection and its feedbacks on the environment. This permits the exploration of deep convection effects on the environment using the ESA approach. A number of forecast metrics have been evaluated for each of the three MPEX cases; only the metrics with the notable sensitivities are reported below.

a. 29 May ESA

Several initial condition variables relevant to an MCS are used in an ESA with a forecast metric (listed in Table 3). All forecasts on 29 May are initialized at 2130 UTC to allow storm spinup via radar data assimilation that begins at 1700 UTC (Table 2). Results indicate that the sensitivity of storm-averaged composite reflectivity ($>20\,\mathrm{dB}Z$) to 850-hPa wind speed reveals a negative sensitivity just east of the initial condition storm location (Figs. 5a,b). Magnitudes of sensitivity exceed $0.4\,\mathrm{dB}Z\,(\mathrm{m\,s^{-1}})^{-1}$ in this region for both a 1-h forecast (Fig. 5a) and a 2-h forecast (Fig. 5b). These negative sensitivities indicate that slower 850-hPa wind speeds in these areas (which are generally downstream of the initial condition storm location) result in higher storm-averaged reflectivity. From the model data, it is evident this is a result of outflow strength's (speed) relationship with the environmental wind profile. In ensemble members with lower forecast reflectivity, the 850-hPa downstream wind has a westerly component while the wind in members with higher reflectivity has an easterly component (not shown). Members with deeper inflow layers also have deeper MCS outflow (not shown). In this case, members with a deeper inflow layer tend to have slower winds at 850 hPa. This is likely case specific and should not be generalized. The positive sensitivities behind the dryline indicate that a faster moving dryline will result in higher reflectivity, likely due to increased lift.

An initial condition difference between ensemble members with the highest and lowest forecast response can support sensitivity results and help distinguish dynamical features from statistical noise. The 850-hPa wind initial condition difference at statistically significant sensitivity grid points is negative in some areas downstream of the initial MCS position (Figs. 6a,b). There are also strong positive differences along the leading edge of the MCS, meaning faster outflow is associated with higher storm reflectivity by increasing convergence.

Forecast average reflectivity is positively sensitive to initial condition 850-hPa temperature (Figs. 5c,d). We hypothesize that warmer low-level temperatures lead to larger CAPE and higher updraft velocities, resulting in higher reflectivity. Initial condition differences between the highest and lowest forecast response show a similar relationship (Figs. 6c,d).

Reflectivity sensitivity to 850-hPa water vapor mixing ratio also shows a positive sensitivity within the inflow region to the east and southeast of the MCS (Figs. 5e,f). This feature is also evident in the member differences (Figs. 6e,f). Physically, ingested air with higher moisture content should yield larger reflectivity values since moisture increases instability resulting in storms with faster updrafts and larger hail. As the 850-hPa level is just above the boundary layer, the positive sensitivities to temperature and moisture suggest that larger CAPE to the east of the storm yields larger reflectivity. This is intuitive given that instability affects updraft velocity. However, the method used here is not appropriate to determine this given the nonlinear relationship between CAPE and reflectivity (not shown). The negative sensitivities to the west behind the dryline suggest a drier western air mass will also produce more lift as it protrudes into the moist air mass. This affects storm coverage, thus affecting average composite reflectivity.
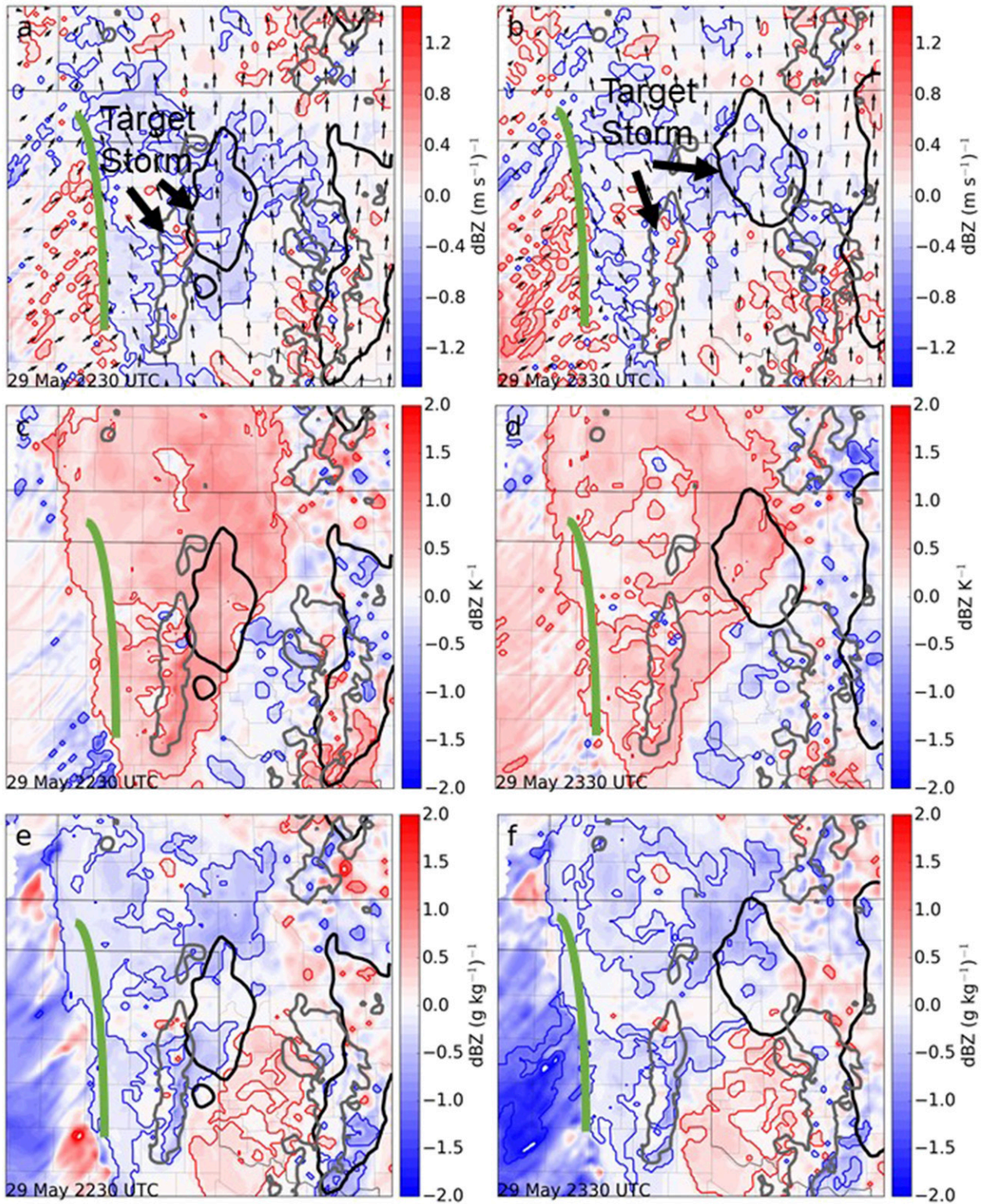
FIG. 5. The 29 May target storm averaged composite reflectivity (>20 dBZ) sensitivity to initial condition 850-hPa wind speed in dBZ (m s^{-1})$^{-1}$, ensemble mean forecasted reflectivity (20 dBZ; black contour), dryline position (green curve), and ensemble mean initial condition reflectivity (20 dBZ; gray contour) and 850-hPa wind vectors for forecast times (a) 1 h, valid at 2230 UTC; and (b) 2 h, valid at 2330 UTC. Next, target storm averaged composite reflectivity (>20 dBZ) sensitivity to initial condition 850-hPa temperature in dBZ K^{-1} for forecast times (c) 1 h, valid at 2230 UTC; and (d) 2 h, valid at 2330 UTC. Last, target storm averaged composite reflectivity (>20 dBZ) sensitivity to initial condition 850-hPa water vapor mixing ratio in dBZ (g kg^{-1})$^{-1}$ for forecast times (e) 1 h, valid at 2230 UTC; and (f) 2 h, valid at 2330 UTC.
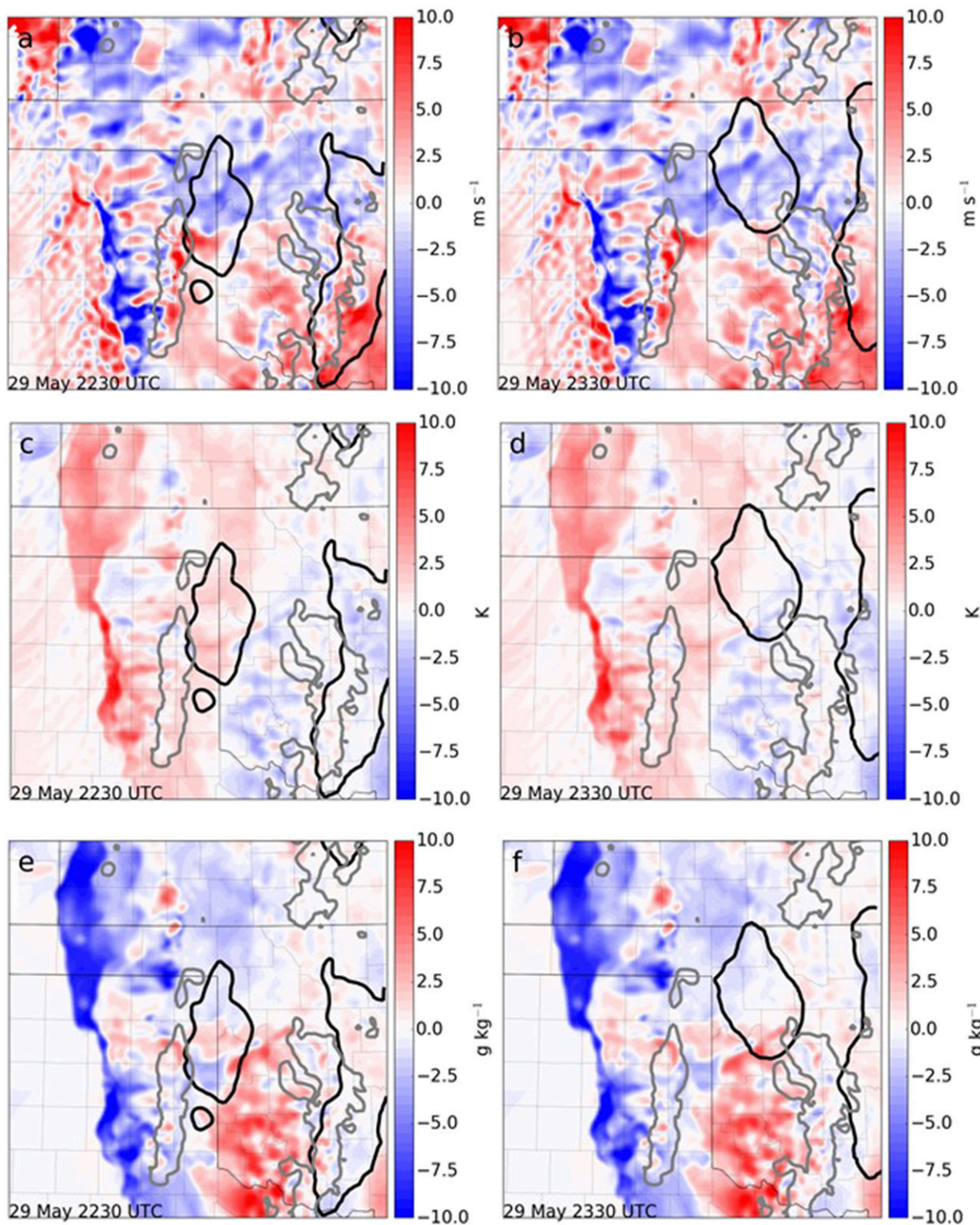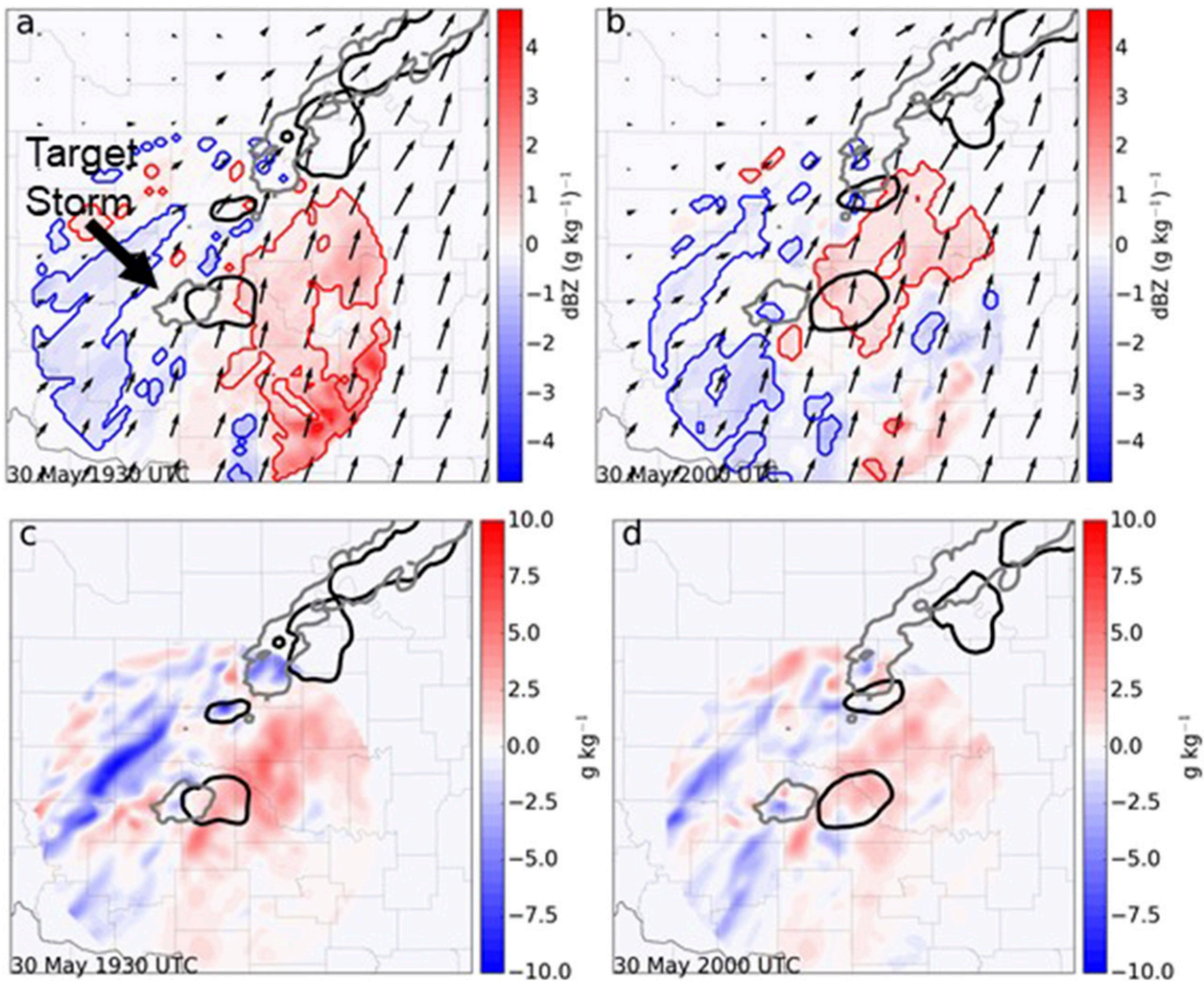
FIG. 6. The 29 May initial condition 850-hPa wind speed difference of members with highest and lowest composite reflectivity forecast response (m s^{-1}) at statistically significant ESA points, ensemble mean forecasted reflectivity (20 dBZ; black contour), and ensemble mean initial condition reflectivity (20 dBZ; gray contour) for forecast times (a) 1 h, valid at 2230 UTC; and (b) 2 h, valid at 2330 UTC. Next, initial condition 850-hPa temperature difference (K) for forecast times (c) 1 h, valid at 2230 UTC; and (d) 2 h, valid at 2330 UTC. Last, initial condition 850-hPa water vapor mixing ratio difference in (g kg^{-1}) for forecast times (e) 1 h, valid at 2230 UTC; and (f) 2 h, valid at 2330 UTC.

FIG. 7. The 30 May target storm averaged composite reflectivity (>20 dBZ) sensitivity (statistically significant outlined) to initial condition 850-hPa water vapor mixing ratio in dBZ $(g\,kg^{-1})^{-1}$, ensemble mean forecasted reflectivity (20 dBZ; black contour), and ensemble mean initial condition reflectivity (20 dBZ; gray contour) and low-level wind vectors for forecast times (a) 30 min, valid at 1930 UTC; and (b) 1 h, valid at 2000 UTC. Initial condition 850-hPa water vapor mixing ratio difference of members with highest and lowest composite reflectivity forecast response $(g\,kg^{-1})$ at statistically significant ESA points for forecast times (c) 30 min, valid at 1930 UTC; and (d) 1 h, valid at 2000 UTC. Sensitivity radius is applied.

b. 30 May ESA

The analysis is next applied to the nontornadic supercell in central Oklahoma on 30 May. For this case, 30- and 60-min forecasts are initialized at 1900 UTC, two hours after convection initiation. Results suggest that storm-averaged composite reflectivity is positively sensitive to low-level moisture within the inflow region and immediately downstream (850 hPa; Figs. 7a,b), most notably for a 30-min forecast. Values are approximately 1 dBZ $(g\,kg^{-1})^{-1}$ in most locations. Ensemble member differences of 850-hPa water vapor mixing ratio (Figs. 7c,d) agree with the positive sensitivity fields in the near-inflow and downstream regions. As in the 29 May case, higher low-level moisture content produces higher reflectivity.

Since one characteristic of a supercell is a persistent, rotating updraft, ESA is applied to the storm 2–5-km UH. For this particular supercell and model grid spacing, ensemble mean UH values are quite small, as some ensemble members only have a maximum UH of 5–$10\,m^2\,s^{-2}$ while the range of average UH within the storm across the ensemble is approximately $45\,m^2\,s^{-2}$. Forecasted storm-averaged UH is found to be sensitive to initial condition 0–6-km bulk vertical wind shear (hereafter SHR06; Figs. 8a,b and 9a,b). Positive sensitivity spans the storm inflow environment to the south and southeast of the storm for both 30- and 60-min forecasts where
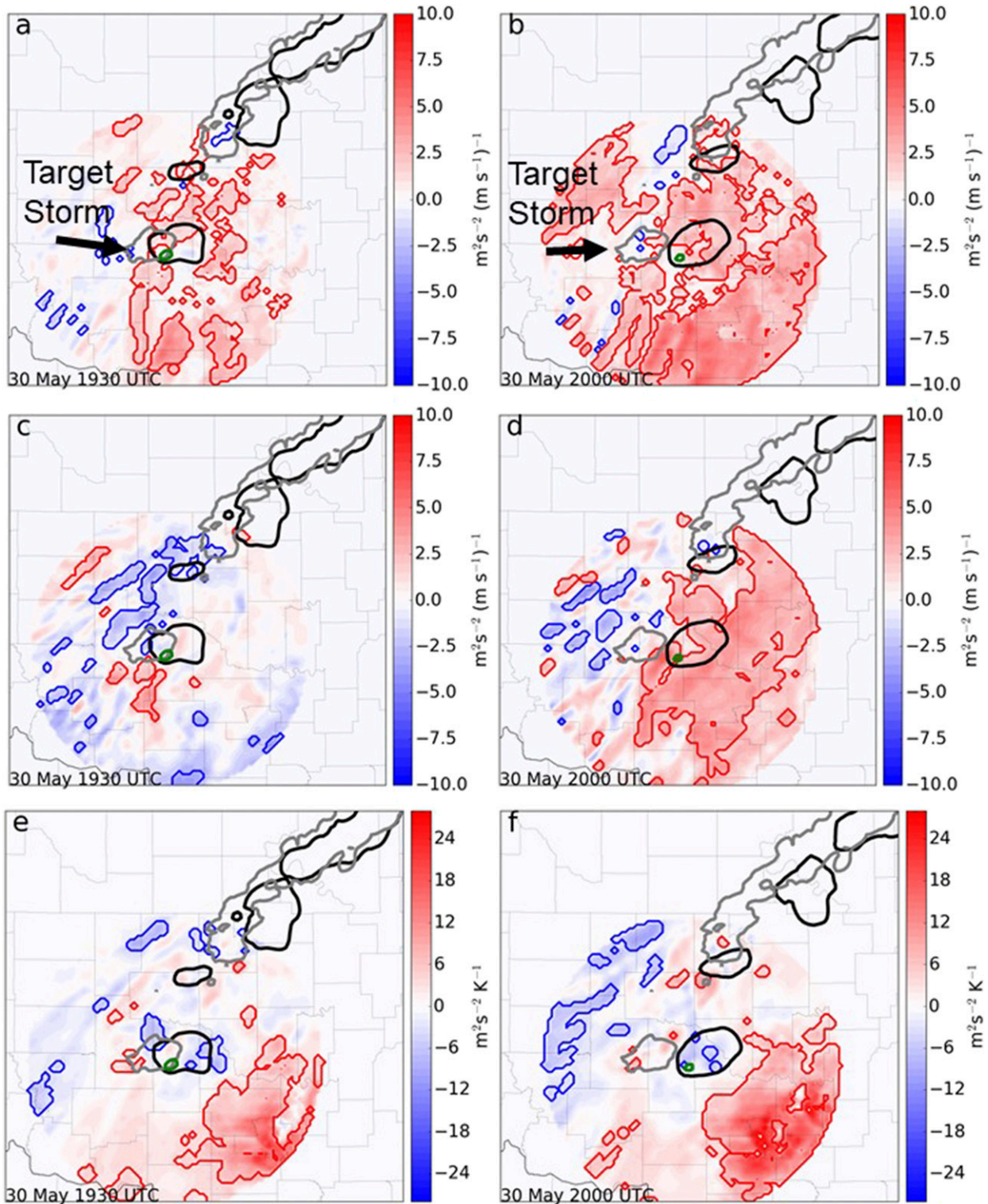
FIG. 8. The 30 May target storm averaged 2–5-km UH ($>5\,\mathrm{m^2\,s^{-2}}$) sensitivity (statistically significant outlined) to initial condition SHR06 in $\mathrm{m^2\,s^{-2}\,(m\,s^{-1})^{-1}}$, ensemble mean forecasted reflectivity (20 dBZ; black contour), 2–5-km UH (5 $\mathrm{m^2\,s^{-2}}$; green contour), and ensemble mean initial condition reflectivity (20 dBZ; gray contour) for forecast times (a) 30 min, valid at 1930 UTC; and (b) 1 h, valid at 2000 UTC. Next, target storm averaged 2–5-km UH ($>5\,\mathrm{m^2\,s^{-2}}$) sensitivity to initial condition 850-hPa wind speed in $\mathrm{m^2\,s^{-2}\,(m\,s^{-1})^{-1}}$ for forecast times (c) 30 min, valid at 1930 UTC; and (d) 1 h, valid at 2000 UTC. Last, target storm averaged 2–5-km UH ($>5\,\mathrm{m^2\,s^{-2}}$) sensitivity to initial condition 850-hPa temperature $\mathrm{m^2\,s^{-2}\,K^{-1}}$ for forecast times (e) 30 min, valid at 1930 UTC; and (f) 1 h, valid at 2000 UTC. Sensitivity radius is applied.
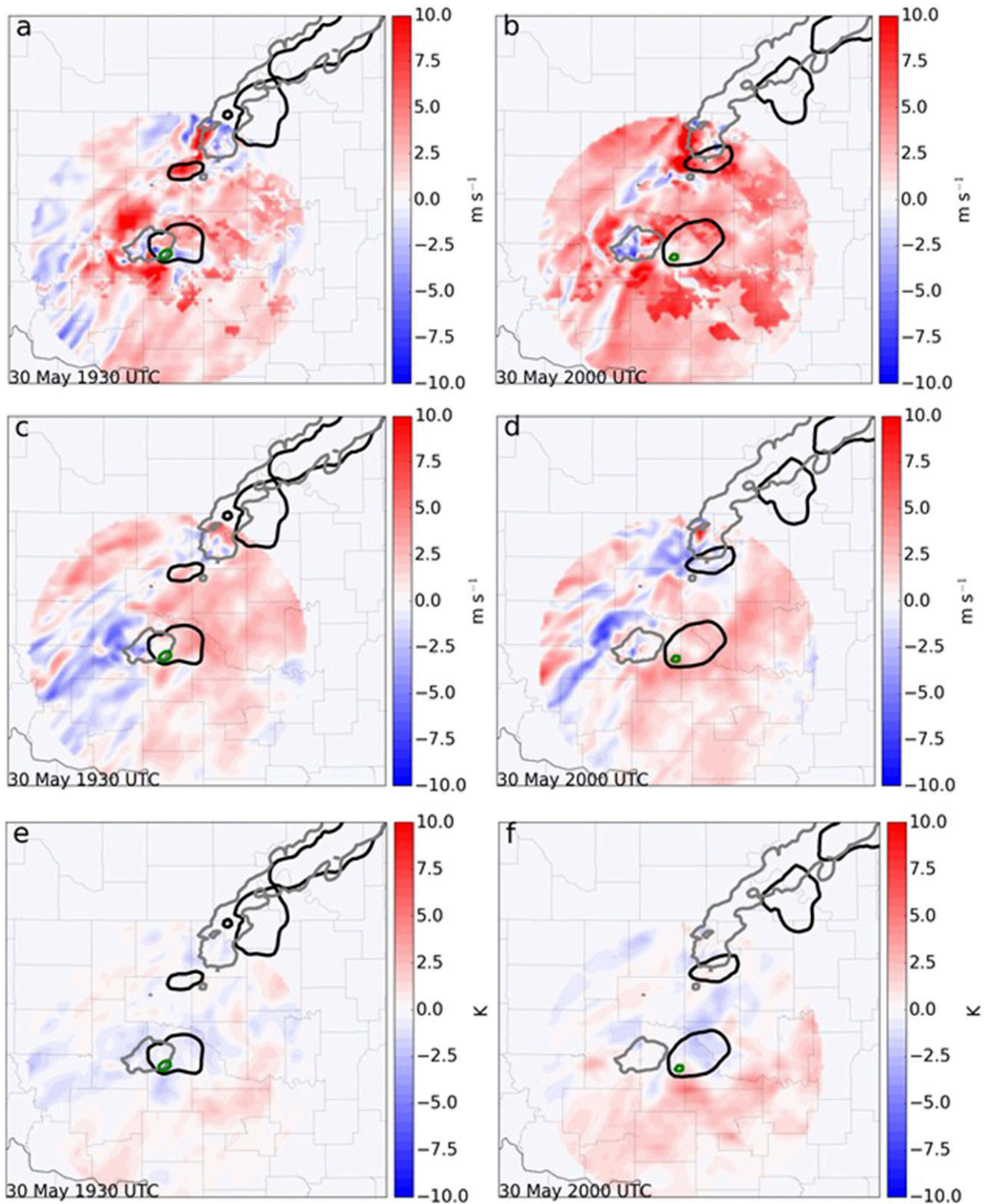
FIG. 9. The 30 May initial condition SHR06 difference of members with highest and lowest 2–5-km UH forecast response (m s^{-1}) at statistically significant ESA points, ensemble mean forecasted reflectivity (20 dB*Z*; black contour), 2–5-km UH (5 m^2 s^{-2}; green contour), and ensemble mean initial condition reflectivity (20 dB*Z*; gray contour) for forecast times (a) 30 min, valid at 1930 UTC; and (b) 1 h, valid at 2000 UTC. Next, initial condition 850-hPa wind speed difference (m s^{-1}) for forecast times (c) 30 min, valid at 1930 UTC; and (d) 1 h, valid at 2000 UTC. Last, initial condition 850-hPa temperature difference (K) for forecast times (e) 30 min, valid at 1930 UTC; and (f) 1 h, valid at 2000 UTC. Sensitivity radius is applied.
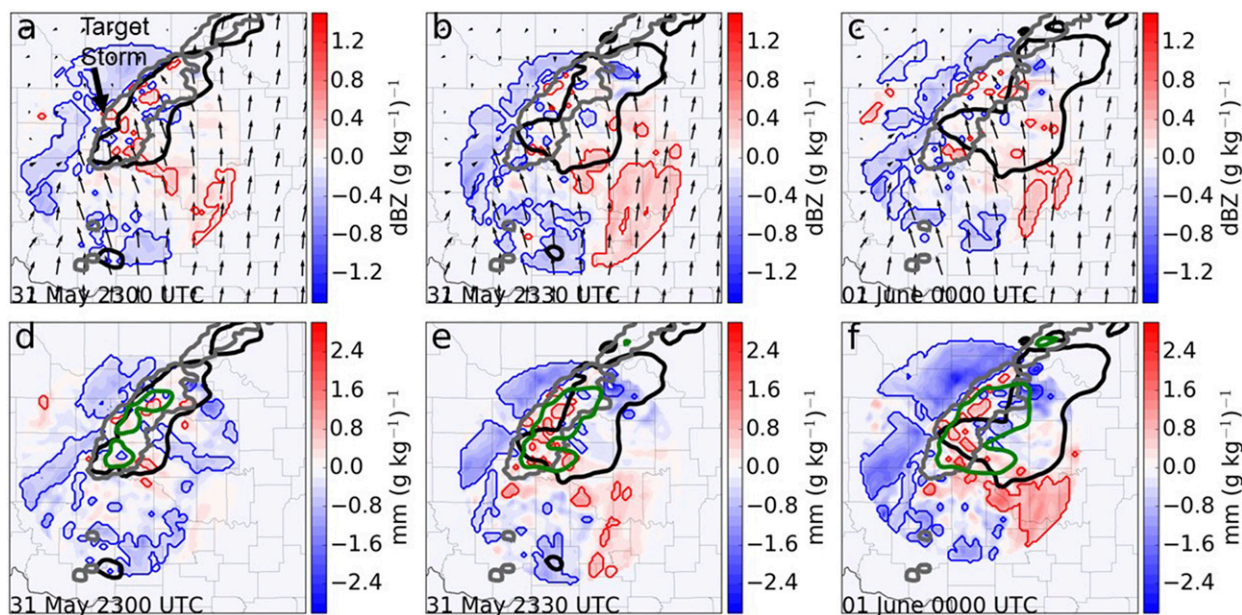
FIG. 10. The 31 May target storm averaged composite reflectivity (>20 dBZ) sensitivity (statistically significant outlined) to initial condition 850-hPa water vapor mixing ratio in dBZ (g kg^{-1})$^{-1}$, ensemble mean forecasted reflectivity (20 dBZ; black contour), and ensemble mean initial condition reflectivity (20 dBZ; gray contour) and low-level wind vectors for forecast times (a) 30 min, valid at 2300 UTC; (b) 1 h, valid at 2330 UTC; and (c) 90 min, valid at 0000 UTC 1 Jun. Also, target storm averaged accumulated rainfall (>10 mm) sensitivity to initial condition 850-hPa water vapor mixing ratio in mm (g kg^{-1})$^{-1}$ with accumulated rainfall (10 mm; green contour) for forecast times (d) 30 min, valid at 2300 UTC; (e) 1 h, valid at 2330 UTC; and (f) 90 min, valid at 0000 UTC 1 Jun. Sensitivity radius is applied.

sensitivity values exceed $7.5 \, \mathrm{m}^2 \, \mathrm{s}^{-2} \, (\mathrm{m \, s}^{-1})^{-1}$. This suggests that larger SHR06 values within the inflow region yield large average UH for this supercell, perhaps even doubling the UH magnitude if SHR06 is increased by just $1 \, \mathrm{m \, s}^{-1}$. An environment of higher inflow vertical wind shear should increase the vorticity of an updraft, thus increasing UH.

Storm UH is also positively sensitive to 850-hPa wind speed, especially within the inflow region for a 60-min forecast where UH has a higher magnitude (Figs. 8c,d and 9c,d). This is more evident for a 60-min forecast since sensitivities are weak in a 30-min forecast. In this 60-min forecast, sensitivity magnitudes exceed $5 \, \mathrm{m}^2 \, \mathrm{s}^{-2} \, (\mathrm{m \, s}^{-1})^{-1}$ within the inflow region. This translates to stronger storm-relative inflow inducing much larger UH. Faster inflow wind speed is directly related to updraft velocity and stretching, where stronger updrafts produce larger UH. The metric also is positively sensitive to 850-hPa temperature within the inflow region (Figs. 8e,f and 9e,f). The results suggest that warmer inflow winds increase updraft speed via changes to updraft parcel buoyancy. There would also be increased baroclinicity normal to the storm motion that may increase UH. In summary, UH will increase if low-level inflow winds are faster, air is warmer, and/or SHR06 is greater. Member differences also reflect UH dependency on these

environmental variables. The member with larger storm UH has faster and warmer inflow along with greater environmental shear.

c. 31 May ESA

As in the 29 and 30 May cases, positive sensitivity of forecast reflectivity to 850-hPa water vapor mixing ratio is prevalent within the inflow region to the southeast of the supercell in the 30-, 60-, and 90-min forecasts (Figs. 10a–c). Negative sensitivities exist to the west behind the boundary (evident through the wind vector analysis). These patterns are also present in the ensemble member differences (Figs. 11a–c), although the difference for a 90-min lead time does not show a positive relationship in the inflow region. Since the 31 May event produced significant flash flooding, ESA is applied to forecast accumulated rainfall. This reveals positive sensitivity to low-level water vapor mixing ratio within the storm inflow region for a 60- and 90-min forecast (Figs. 10e,f and 11e,f). Storm-ingested water vapor originating from the moist air mass to the east of the storm is seen to directly impact rainfall amounts. These sensitivity values are 1.6–2.4 mm (g kg^{-1})$^{-1}$. Overall, these results are similar in structure to the reflectivity sensitivities, which is to be expected.
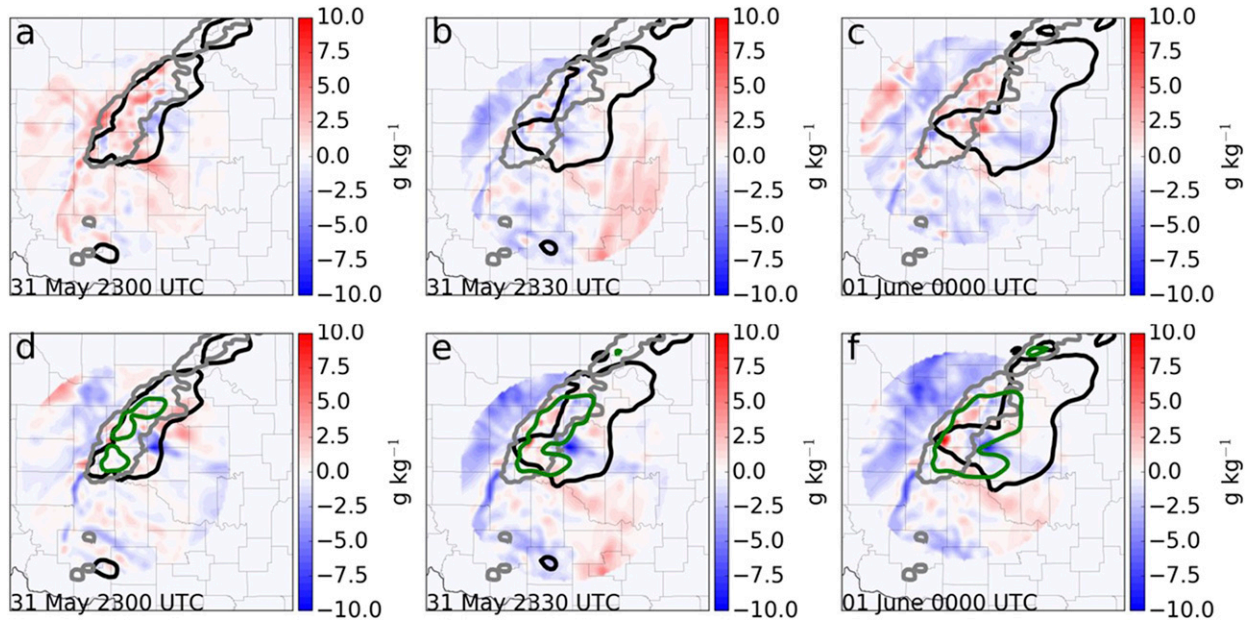
FIG. 11. The 31 May initial condition 850-hPa water vapor mixing ratio difference of members with the highest and lowest composite reflectivity forecast response (g kg^{-1}) at statistically significant ESA points, ensemble mean forecasted reflectivity (20 dBZ; black contour), and ensemble mean initial condition reflectivity (20 dBZ; gray contour) for forecast times (a) 30 min, valid at 2300 UTC; (b) 1 h, valid at 2330 UTC; and (c) 90 min, valid at 0000 UTC 1 Jun. Also, initial condition 850-hPa water vapor mixing ratio difference of members with highest and lowest accumulated rainfall forecast response (g kg^{-1}) with accumulated rainfall (10 mm; green contour) for forecast times (d) 30 min, valid at 2300 UTC; (e) 1 h, valid at 2330 UTC; and (f) 90 min, valid at 0000 UTC 1 Jun. Sensitivity radius is applied.

The ESA technique is also applied to the storm 2–5-km UH beginning with SHR06 (Fig. 12), but using a larger UH threshold (75 m^2 s^{-2}) than for the 30 May event (5 m^2 s^{-2}) to remove UH values not associated with the main updraft in this intense storm. Broad areas of positive sensitivity exists within the near inflow region for 30- and 60-min forecasts (Figs. 12a,b,d,e). The sensitivity magnitudes decrease for a 90-min forecast (Figs. 12c,f). As in the 30 May case, larger 0–6-km inflow environmental wind shear increases UH. Sobash et al. (2016) show through verification that 2–5-km UH is a poor surrogate for tornado prediction since it is a measure of midlevel updraft rotation, while low-level rotation provides more insight into tornado probabilities. Thus, 0–1-km UH is also chosen as a forecast metric. The sensitivity of 0–1-km UH to 0–1-km vertical wind shear (hereafter SHR01) indicates that 0–1-km UH is positively sensitive to SHR01 for 15- and 30-min forecasts with values exceeding 1 m^2 s^{-2} (m s^{-1})$^{-1}$ for the 30-min forecast (Fig. 13). The positive sensitivities are found in the inflow region close to the storm. Increased low-level shear within the inflow region increases low-level UH.

d. Sensitivity to vertical wind shear feedbacks

Brooks et al. (1994) demonstrate how the vertical wind profile is modified within the inflow of an idealized supercell simulation out to distances of several tens of kilometers. In the present study, convective perturbations to SHR06 in supercell inflow regions are analyzed. Changes in vertical wind shear due to convective feedbacks on 30 May indicate that wind shear is enhanced to the southeast of the target supercell in central Oklahoma by magnitudes less than 10 m s^{-1}, while nontargeted convection to the north also impacts the mesoscale environment in other areas (Fig. 14). The target supercell's shear enhancement does not extend very far from the storm. Shear is also enhanced, and by greater magnitudes (~10–12 m s^{-1}), within the lingering cold pool of the targeted supercell storm. For the 31 May case, however, the enhancement of inflow SHR06 and SHR01 to the south and southeast of the storm is notable in both magnitude and areal extent (Fig. 15); the inflow SHR06 increases by 15–20 m s^{-1} over a 60-min period and extends outward from the storm (Fig. 15b). Inflow SHR01 increases as well within the inflow region (Figs. 15c,d). These results overall suggest environmental shear perturbations are sensitive to supercell updraft strength and consequential storm size.

Like many previous studies, this study shows that vertical wind shear is convectively enhanced within the inflow region of supercells. Since UH has been shown to be positively sensitive to shear within the inflow region, these short-term impacts on the environment caused by convection could be an important feedback to
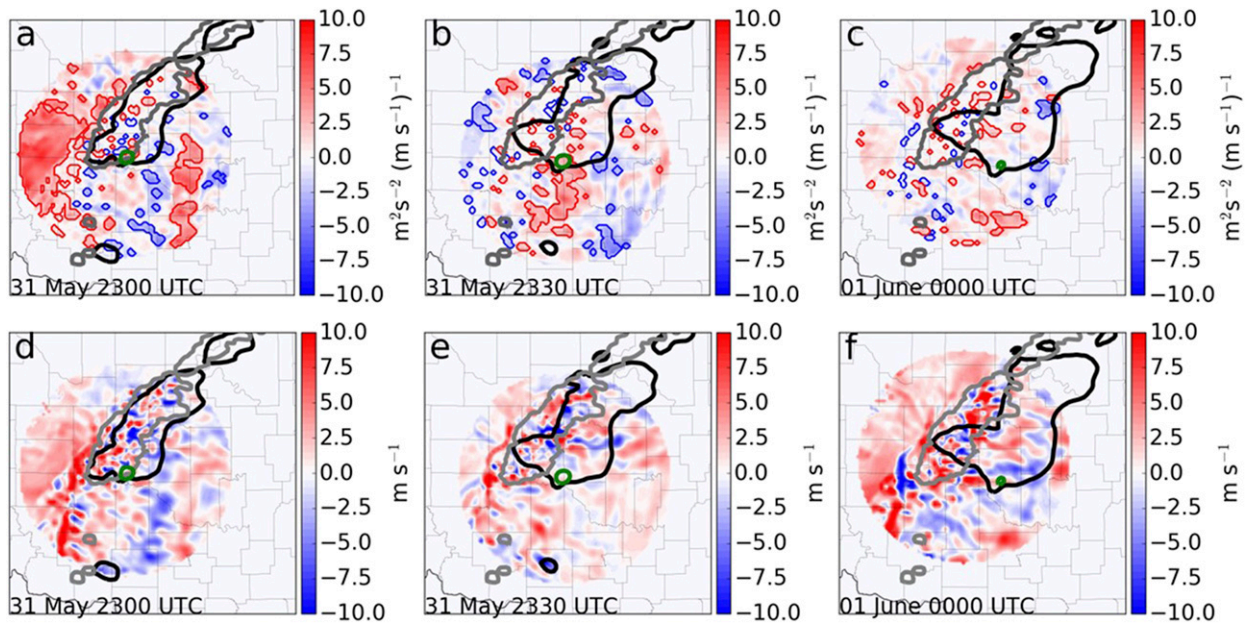
FIG. 12. The 31 May target storm averaged 2–5-km UH ($>75\,\mathrm{m}^2\,\mathrm{s}^{-2}$) sensitivity (statistically significant outlined) to initial condition SHR06 in $\mathrm{m}^2\,\mathrm{s}^{-2}\,(\mathrm{m}\,\mathrm{s}^{-1})^{-1}$, ensemble mean forecasted reflectivity (20 dBZ; black contour), 2–5-km UH (75 $\mathrm{m}^2\,\mathrm{s}^{-2}$; green contour), and ensemble mean initial condition reflectivity (20 dBZ; gray contour) for forecast times (a) 30 min, valid at 2300 UTC; (b) 1 h, valid at 2330 UTC; and (c) 90 min, valid at 0000 UTC. Also, initial condition SHR06 difference of members with highest and lowest 2–5-km UH forecast response ($\mathrm{m}\,\mathrm{s}^{-1}$) at statistically significant ESA points for forecast times (d) 30 min, valid at 2300 UTC; (e) 1 h, valid at 2330 UTC; and (f) 90 min, valid at 0000 UTC 1 Jun. Sensitivity radius is applied.

convection evolution. Thus, ESA is once again applied to UH, however, the "initial condition" x is the *change* in wind shear over a 1-h time period. This change in wind shear is determined using the method described in section 2d. Using this change metric, positive (negative) sensitivities represent scenarios where short-term increases (decreases) in vertical wind shear caused by the supercell storm lead to larger storm UH in the future. Statistical significance testing is less useful here given the nonlinear relationship between convective perturbations and forecast metrics; however, the linear response qualitatively represents the correlations.

Beginning with the 30 May case, results indicate that 2–5-km UH is positively sensitive to the 60-min storm-induced changes in SHR06 (1800–1900 UTC) in a small area to the south and west of the supercell for the 30-min forecast (Fig. 16), with the strongest sensitivity for the 60-min forecast. This suggests that the storm-induced increases in SHR06 have an effect on future convection evolution, meaning some positive feedback exists between this storm and the environment, and that this feedback appears to occur over a 60-min time period.

The 31 May results show a similar feedback pattern. Results show that there is only a weak area of positive sensitivity to 2–5-km UH from the 60-min storm-induced change in SHR06 for the 30-min forecast

directly south of the updraft (Fig. 17a), with a much larger and stronger region of positive sensitivity for the 60-min forecast (2130–2230 UTC). Both forecast times have these positive sensitivities to the south of the storm in the inflow region (Fig. 17). This positive sensitivity within the inflow regions again supports the idea of positive feedback between the storm and its nearby environment, with an inherent time scale for how long it takes the environmental changes to feed back and influence supercell structure. This feedback time scale appears to be around 60 min. This feedback is likely more prevalent on 31 May because the storm perturbs the environment to a greater extent than seen on 30 May. Positive feedback on low-level mesocyclone strength, as defined by the 0–1-km UH, is also present where inflow SHR01 is enhanced by convection (Fig. 18), but the time scale is shorter. This feedback is best seen for a 30-min forecast, with the 15- and 45-min forecasts showing weaker sensitivity. Thus, the supercell low-level rotation is positively sensitive to enhancements of SHR01 within the inflow region.

4. Discussion and conclusions

The results of this study reveal how convection evolution is dependent on the surrounding near-storm
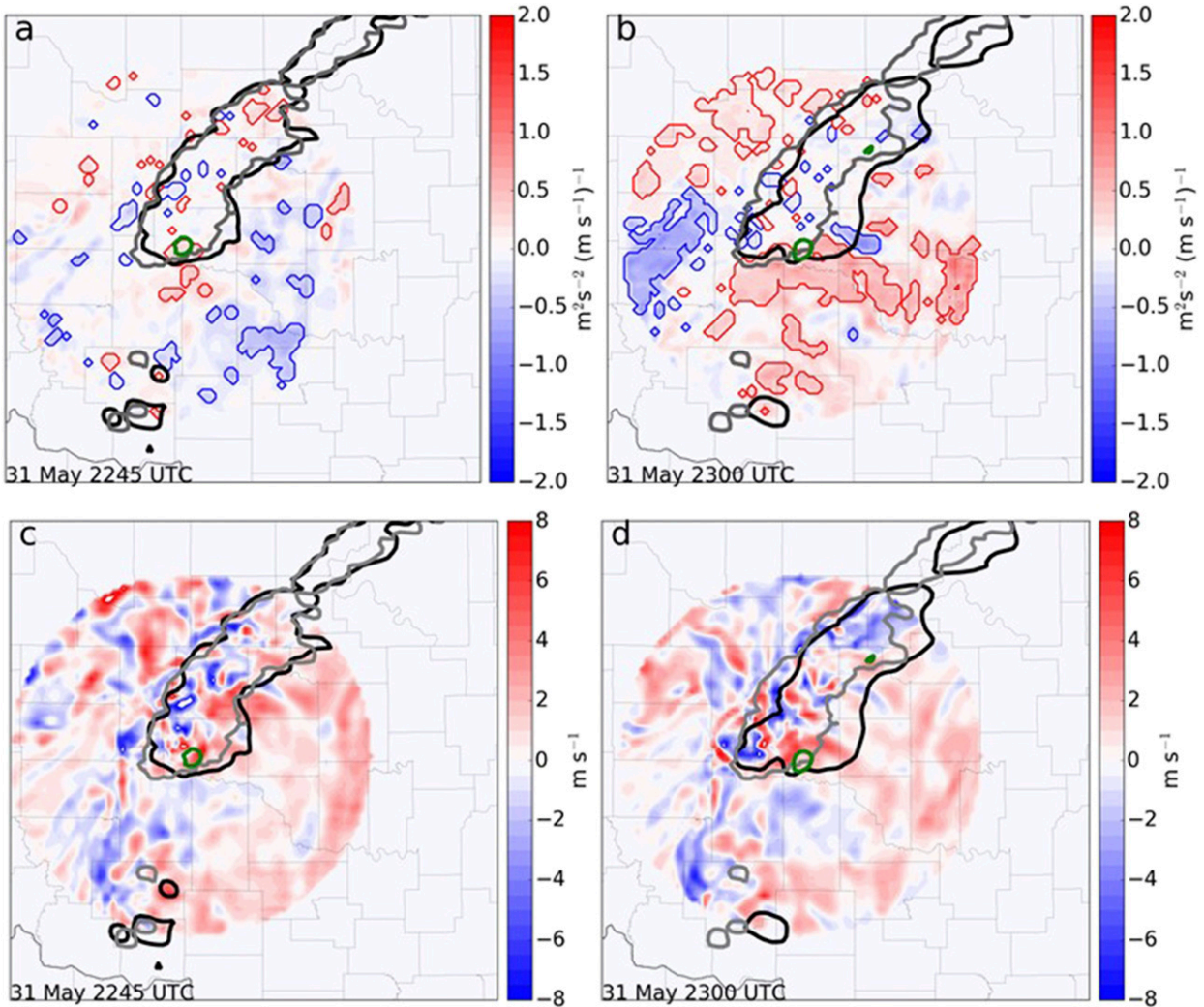
FIG. 13. The 31 May target storm averaged 0–1-km UH ($>5\,m^2\,s^{-2}$) sensitivity (statistically significant outlined) to initial condition SHR01 in $m^2\,s^{-2}\,(m\,s^{-1})^{-1}$ and ensemble mean forecasted reflectivity (20 dBZ; black contour) and 0–1-km UH ($5\,m^2\,s^{-2}$; green contour) and ensemble mean initial condition reflectivity (20 dBZ; gray contour) for forecast times (a) 15 min, valid at 2245 UTC; and (b) 30 min, valid at 2300 UTC. Also, initial condition SHR01 difference of members with highest and lowest 0–1-km UH forecast response ($m\,s^{-1}$) at statistically significant ESA points for forecast times (c) 15 min, valid at 2245 UTC; and (d) 30 min, valid at 2300 UTC. Sensitivity radius is applied.

environment. Many relationships are presented between storm forecast metrics and environmental variables, and similarities are seen among the three cases. Reflectivity and rainfall accumulation are dependent on low-level environmental moisture, particularly within the inflow region. Higher environmental water vapor content results in higher reflectivity and rainfall accumulation. Along with low-level humidity, low-level temperature also affects the storms by increasing lifted parcel buoyancy. Reflectivity and updraft rotation are both enhanced by warmer low-level temperatures, likely due to larger parcel buoyancy producing a stronger updraft. Low-level inflow winds impact supercell evolution

by increasing UH intensity via updraft intensification and stretching. Inflow environmental vertical wind shear increases updraft helicity in both the nontornadic and tornadic supercell cases in this study (Figs. 8a,b and 12a–c). Overall, the three cases highlight the influence of the inflow and downstream environments on convection evolution for both supercells and convective lines.

A method to investigate storm–environment feedbacks is presented that indicates positive feedbacks between supercell thunderstorms and their surrounding environments. Since vertical wind shear is enhanced within supercell inflow regions and supercell rotation is affected by environmental vertical wind shear, the
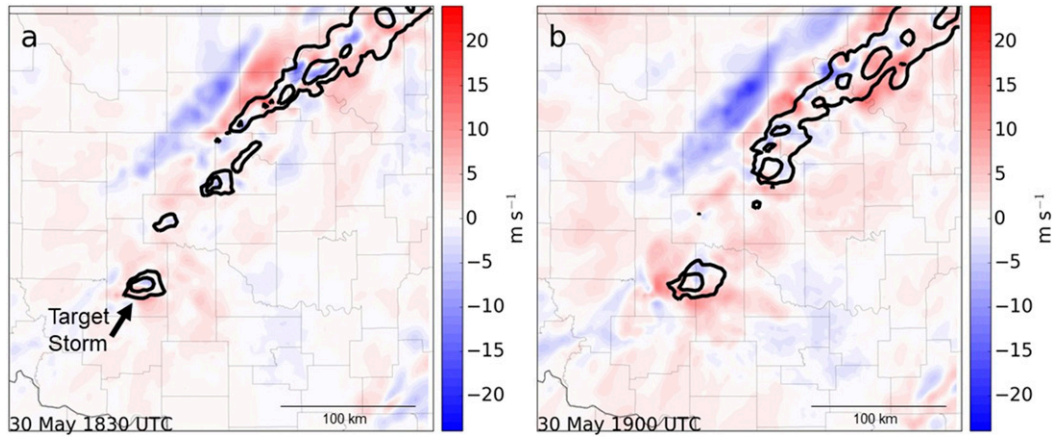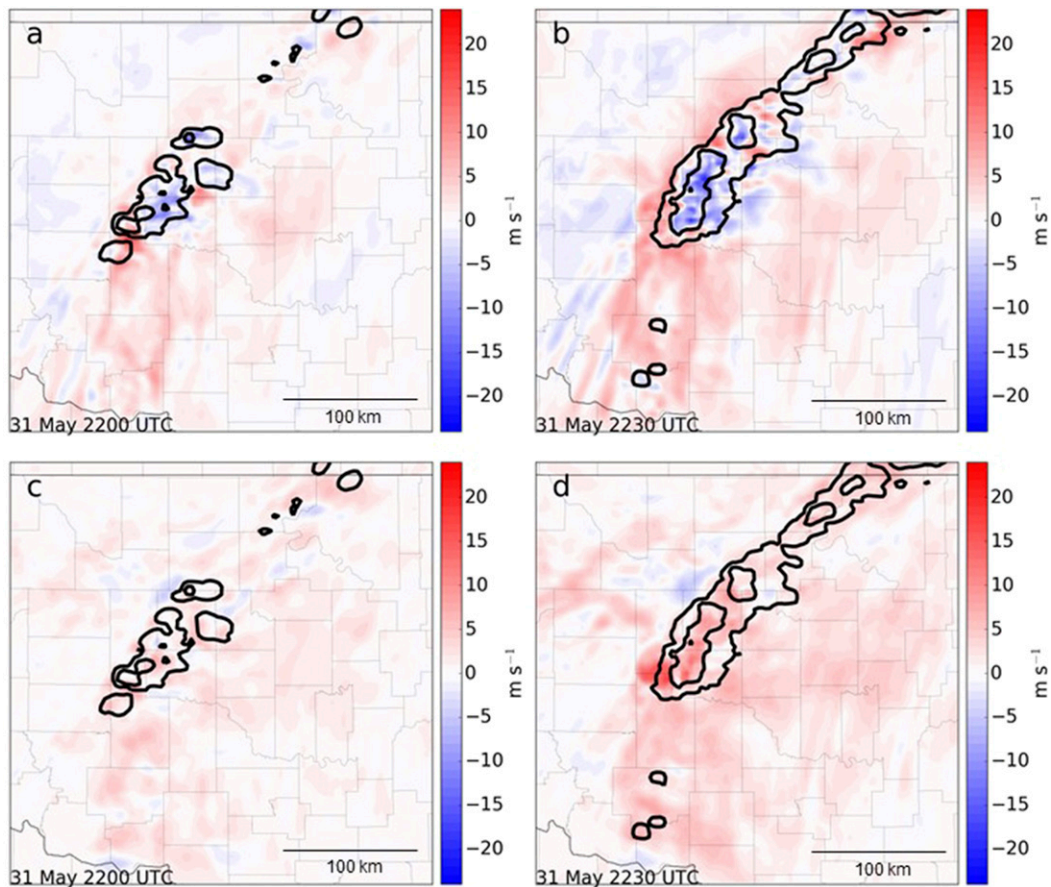
FIG. 14. The 30 May 2013 ensemble mean analysis SHR06 difference in m s^{-1} from 1800 UTC due to convection (filled) and low-level reflectivity (20-dBZ intervals) at (a) 1830 and (b) 1900 UTC.

storm-induced enhancements of wind shear result in larger storm UH at a later time. Results further suggest that the time scale for this feedback process is on the order of an hour. This effect is stronger in the tornadic

supercell of 31 May than the nontornadic supercell of 30 May given the greater magnitude and spatial extent (~100 km) of vertical wind shear perturbations. A possible explanation for this difference is outlined by

FIG. 15. The 31 May 2013 ensemble mean analysis SHR06 difference in m s^{-1} from 2130 UTC due to convection (filled) and low-level reflectivity (20-dBZ intervals) at (a) 2200 UTC, (b) 2230 UTC, (c) SHR01 difference at 2200 UTC, and (d) SHR01 difference at 2230 UTC.
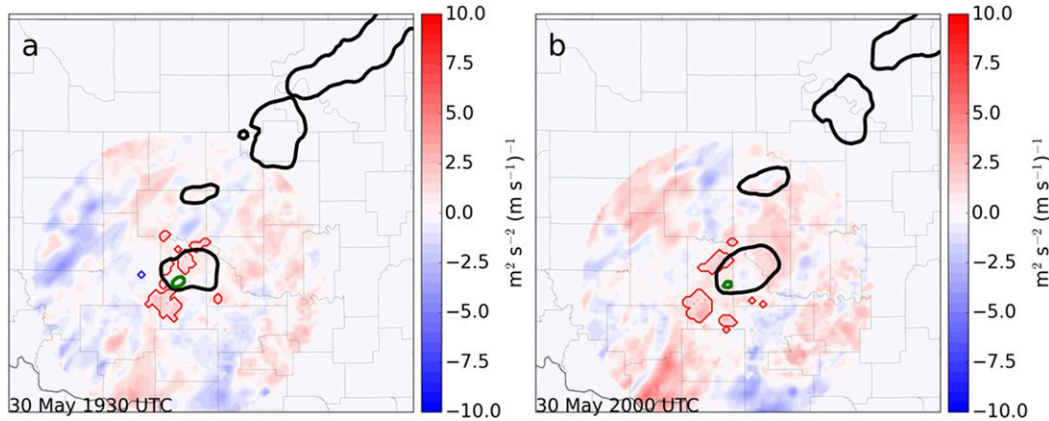
FIG. 16. The 30 May target storm averaged 2–5-km UH ($>5\,\mathrm{m^2\,s^{-2}}$) sensitivity (statistically significant outlined) to initial 1-h storm-induced change of SHR06 in $\mathrm{m^2\,s^{-2}\,(m\,s^{-1})^{-1}}$ and ensemble mean forecasted reflectivity (20 dBZ; black contour) and 2–5-km UH ($5\,\mathrm{m^2\,s^{-2}}$; green contour) for forecast times (a) 30 min, valid at 1930 UTC; and (b) 1 h, valid at 2000 UTC. Sensitivity radius is applied.

Morrison (2016a,b). Updraft-induced perturbation horizontal pressure gradient magnitudes are directly proportional to CAPE. This translates to enhanced vertical wind shear within the vicinity of convection. The preconvective environmental CAPE on 31 May is significantly higher compared to 30 May ($\sim$5000 vs $\sim$2000 J kg^{-1}; not shown). Thus, greater vertical wind shear perturbations on 31 May are expected and may lead to more pronounced storm–environment feedbacks. This feedback could be a crucial part of mesocyclone maintenance and intensity and deserves further study. Results also suggest a feedback between storm-induced changes to the 0–1-km vertical wind shear in the inflow region and low-level mesocyclone strength, which acts on a time scale of approximately 30 min. The shorter

time scale is reasonable, as the storm-induced 0–1-km wind shear changes occur closer to the storm. While some of these sensitivities may arise from initial storm strength since stronger storms will perturb the environment more and perhaps have larger forecasted UH, this feedback can be theorized through deductive reasoning: 1) supercells enhance inflow shear, 2) UH evolution is sensitive to inflow shear, and 3) UH evolution is sensitive to inflow shear enhancements.

The ESA results suggest that it is imperative for the near-storm environment to be reasonably well represented in CAM initial conditions, especially in regions of high forecast sensitivity. Model biases for different state variables, as shown by Kerr et al. (2017), can degrade the accuracy of model initial conditions. Thus, model biases
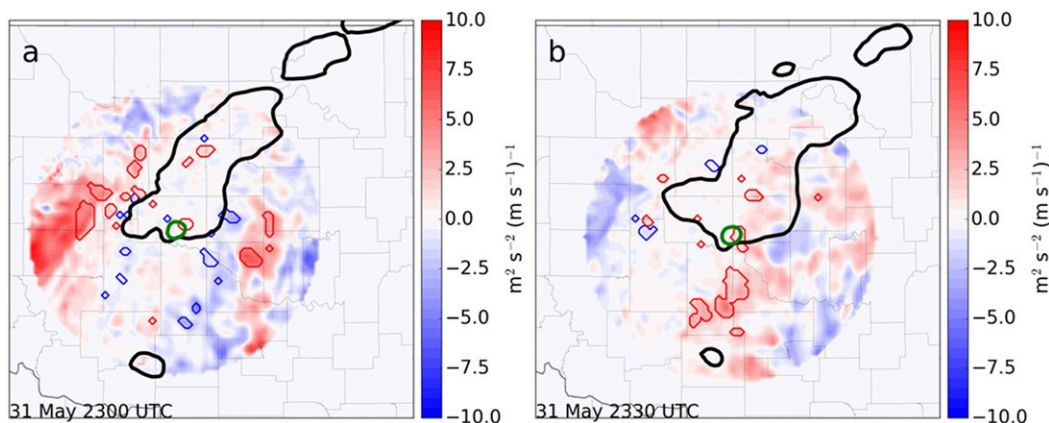

FIG. 17. The 31 May target storm averaged 2–5-km UH ($>75\,\mathrm{m^2\,s^{-2}}$) sensitivity (statistically significant outlined) to initial 1-h storm-induced change of SHR06 in $\mathrm{m^2\,s^{-2}\,(m\,s^{-1})^{-1}}$ and ensemble mean forecasted reflectivity (20 dBZ; black contour) and 2–5-km UH ($75\,\mathrm{m^2\,s^{-2}}$; green contour) for forecast times (a) 30 min, valid at 2300 UTC; and (b) 1 h, valid at 2330 UTC. Sensitivity radius is applied.
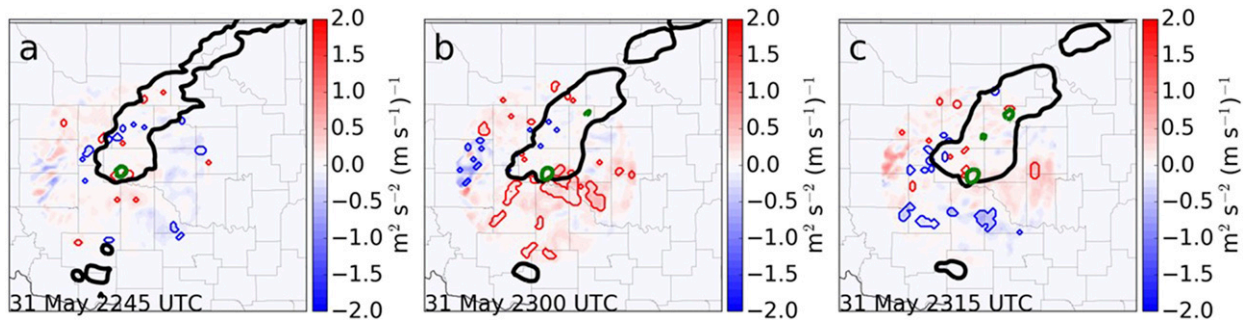
FIG. 18. The 31 May target storm averaged 0–1-km UH ($>5\,\mathrm{m^2\,s^{-2}}$) sensitivity (statistically significant outlined) to initial 1-h storm-induced change of SHR01 in $\mathrm{m^2\,s^{-2}\,(m\,s^{-1})^{-1}}$ and ensemble mean forecasted reflectivity (20 dBZ; black contour) and 0–1-km UH ($5\,\mathrm{m^2\,s^{-2}}$; green contour) for forecast times (a) 15 min, valid at 2245 UTC; (b) 30 min, valid at 2300 UTC; and (c) 45 min, valid at 2315 UTC. Sensitivity radius is applied.

in areas of high forecast sensitivity can have negative effects on forecast accuracy. The following are potential model biases that may impact forecasts based on ESA:

1) Underdepicted low-level storm inflow wind speed could affect supercell UH and multicell reflectivity. Since supercell UH in these cases is positively sensitive to inflow wind speed, an underdepiction of initial condition inflow winds should lead to underestimated forecasted UH. For the 29 May MCS case, the average forecast composite reflectivity is negatively sensitive to low-level inflow wind speed. From these results, it is suggested the underdepiction of inflow winds would produce higher average MCS reflectivity.

2) Comparison of observed and analysis vertical wind shear shows the underdepiction of shear within model analyses caused by the underdepiction of low-level wind speed (Kerr et al. 2017). UH is positively sensitive to inflow vertical wind shear (over varying depths; some not shown) meaning a negative bias in initial condition wind shear would produce weaker forecast UH. For low-level rotation, this underdepiction could be important to tornado probabilities derived from model proxies.

3) ESA applied to the 29 May MCS shows small areas of negative sensitivity along the apex of the gust front for 850-hPa temperature, meaning colder temperatures at these locations are associated with higher reflectivity values. Deeper cold pools would cause their propagation speed to increase, thus resulting in more lift along the gust front.

These results from several ESAs using various forecast metrics and initial condition variables show clearly that low-level environmental features affect short-term convection evolution. Targeted low-level observations (e.g., unmanned aircraft systems) near

convective storms could improve short-term predictions of convection evolution. Clear-air radial velocity observations of near-storm environments may also be beneficial to short-term prediction.

In summary, ESA has been shown to be an effective tool when applied on the storm scale to reveal storm–environment dependencies and feedbacks. Results suggest that ESA must be applied to very short-term forecasts for the linear relationship assumption between initial condition variables and forecast metrics to reveal physical connections. Generally, in this study, the larger the forecasted convective storm, the longer the lead times in which ESA can be reliably applied. Applying ESA to longer-term forecasts, such as 3–6 h, for individual storms may not yield meaningful results as the linear assumption fails. There are also limitations at the time scales presented given the necessary linear assumption. Some sensitivity fields have noisy appearances likely owing to nonlinear relationships between environmental and storm variables. Polynomial regression techniques should be utilized in future studies to improve storm-scale sensitivity analyses. Other future work should include more supercell case studies of various sizes and intensities to further explore storm–environment feedbacks for multiple variables. Since convective events rapidly evolve and require nowcasting, forecasters could use sensitivities to environmental initial conditions coupled with observations within sensitive regions to weight the ensemble member forecasts (Ancell 2016).

REFERENCES

Aksoy, A., D. Dowell, and C. Snyder, 2009: A multicase comparative assessment of the ensemble Kalman filter for assimilation of radar observations. Part I: Storm-scale analyses. *Mon. Wea. Rev.*, **137**, 1805–1824, https://doi.org/10.1175/2008MWR2691.1.

Ancell, B. C., 2016: Improving high-impact forecasts through sensitivity-based ensemble subsets: Demonstration and initial tests. *Wea. Forecasting*, **31**, 1019–1036, https://doi.org/10.1175/WAF-D-15-0121.1.

——, and G. J. Hakim, 2007: Comparing adjoint- and ensemble-sensitivity analysis with applications to observation targeting. *Mon. Wea. Rev.*, **135**, 4117–4134, https://doi.org/10.1175/2007MWR1904.1.

Anderson, J. L., 2001: An ensemble adjustment filter for data assimilation. *Mon. Wea. Rev.*, **129**, 2884–2903, https://doi.org/10.1175/1520-0493(2001)129<2884:AEAKFF>2.0.CO;2.

——, 2007: An adaptive covariance inflation error correction algorithm for ensemble filters. *Tellus*, **59A**, 210–224, https://doi.org/10.1111/j.1600-0870.2006.00216.x.

——, T. Hoar, K. Raeder, H. Liu, N. Collins, R. Torn, and A. Avellano, 2009: The Data Assimilation Research Testbed: A community facility. *Bull. Amer. Meteor. Soc.*, **90**, 1283–1296, https://doi.org/10.1175/2009BAMS2618.1.

Bednarczyk, C. N., and B. C. Ancell, 2015: Ensemble sensitivity analysis applied to a southern plains convective event. *Mon. Wea. Rev.*, **143**, 230–249, https://doi.org/10.1175/MWR-D-13-00321.1.

Berman, J. D., R. D. Torn, G. S. Romine, and M. L. Weisman, 2017: Sensitivity of northern Great Plains convection forecasts to upstream and downstream forecast errors. *Mon. Wea. Rev.*, **145**, 2141–2163, https://doi.org/10.1175/MWR-D-16-0353.1.

Bluestein, H. B., J. C. Snyder, and J. B. Houser, 2015: A multiscale overview of the El Reno, Oklahoma, tornadic supercell of 31 May 2013. *Wea. Forecasting*, **30**, 525–552, https://doi.org/10.1175/WAF-D-14-00152.1.

Brooks, H. E., C. A. Doswell III, and J. Cooper, 1994: On the environments of tornadic and nontornadic mesocyclones. *Wea. Forecasting*, **9**, 606–618, https://doi.org/10.1175/1520-0434(1994)009<0606:OTEOTA>2.0.CO;2.

Cintineo, R. M., and D. J. Stensrud, 2013: On the predictability of supercell thunderstorm evolution. *J. Atmos. Sci.*, **70**, 1993–2011, https://doi.org/10.1175/JAS-D-12-0166.1.

Clark, A. J., W. A. Gallus Jr., M. Xue, and F. Kong, 2010a: Growth of spread in convection-allowing and convection-parameterizing ensembles. *Wea. Forecasting*, **25**, 594–612, https://doi.org/10.1175/2009WAF2222318.1.

——, ——, ——, and ——, 2010b: Convection-allowing and convection-parameterizing ensemble forecasts of a mesoscale convective vortex and associated severe weather environment. *Wea. Forecasting*, **25**, 1052–1081, https://doi.org/10.1175/2010WAF2222390.1.

Coniglio, M. C., S. M. Hitchcock, and K. H. Knopfmeier, 2016: Impact of assimilating preconvective upsonde observations on short-term forecasts of convection observed during MPEX. *Mon. Wea. Rev.*, **144**, 4301–4325, https://doi.org/10.1175/MWR-D-16-0091.1.

Cortinas, J. V., and D. J. Stensrud, 1995: The importance of understanding mesoscale model parameterization schemes for weather forecasting. *Wea. Forecasting*, **10**, 716–740, https://doi.org/10.1175/1520-0434(1995)010<0716:TIOUMM>2.0.CO;2.

Cressman, G. P., 1959: An operational objective analysis system. *Mon. Wea. Rev.*, **87**, 367–374, https://doi.org/10.1175/1520-0493(1959)087<0367:AOOAS>2.0.CO;2.

Dowell, D. C., and L. J. Wicker, 2009: Additive noise for storm-scale ensemble forecasting and data assimilation. *J. Atmos. Oceanic Technol.*, **26**, 911–927, https://doi.org/10.1175/2008JTECHA1156.1.

——, F. Zhang, L. J. Wicker, C. Snyder, and N. A. Crook, 2004: Wind and temperature retrievals in the 17 May 1981 Arcadia, Oklahoma, supercell: Ensemble Kalman filter experiments. *Mon. Wea. Rev.*, **132**, 1982–2005, https://doi.org/10.1175/1520-0493(2004)132<1982:WATRIT>2.0.CO;2.

Flack, D. L. A., S. L. Gray, and R. S. Plant, 2018: Convective-scale perturbation growth across the spectrum of convective regimes. *Mon. Wea. Rev.*, **146**, 387–405, https://doi.org/10.1175/MWR-D-17-0024.1.

Fritsch, J. M., and R. A. Maddox, 1981a: Convectively driven mesoscale pressure systems aloft. Part I: Observations. *J. Appl. Meteor.*, **20**, 9–19, https://doi.org/10.1175/1520-0450(1981)020<0009:CDMWSA>2.0.CO;2.

——, and ——, 1981b: Convective driven mesoscale weather systems aloft. Part II: Numerical simulations. *J. Appl. Meteor.*, **20**, 20–26, https://doi.org/10.1175/1520-0450(1981)020<0020:CDMWSA>2.0.CO;2.

Gaspari, G., and S. E. Cohn, 1999: Construction of correlation functions in two and three dimensions. *Quart. J. Roy. Meteor. Soc.*, **125**, 723–757, https://doi.org/10.1002/qj.49712555417.

Hakim, G. J., and R. D. Torn, 2008: Ensemble synoptic analysis. *Synoptic-Dynamic Meteorology and Weather Analysis and Forecasting: A Tribute to Fred Sanders*, *Meteor. Monogr.*, No. 55, Amer. Meteor. Soc., 147–162.

Hill, A. J., C. C. Weiss, and B. C. Ancell, 2016: Ensemble sensitivity analysis for mesoscale forecasts of dryline convection initiation. *Mon. Wea. Rev.*, **144**, 4161–4182, https://doi.org/10.1175/MWR-D-15-0338.1.

Hitchcock, S. M., M. C. Coniglio, and K. H. Knopfmeier, 2016: Impact of MPEX upsonde observations on ensemble analyses and forecasts of the 31 May 2013 convective event over Oklahoma. *Mon. Wea. Rev.*, **144**, 2889–2913, https://doi.org/10.1175/MWR-D-15-0344.1.

Hohenegger, C., D. Lüthi, and C. Schär, 2006: Predictability mysteries in cloud-resolving models. *Mon. Wea. Rev.*, **134**, 2095–2107, https://doi.org/10.1175/MWR3176.1.

Johnson, A., and X. Wang, 2016: A study of multiscale initial condition perturbation methods for convection-permitting ensemble forecasts. *Mon. Wea. Rev.*, **144**, 2579–2604, https://doi.org/10.1175/MWR-D-16-0056.1.

——, and Coauthors, 2014: Multiscale characteristics and evolution of perturbations for warm season convection-allowing

precipitation forecasts: Dependence on background flow and method of perturbation. *Mon. Wea. Rev.*, **142**, 1053–1073, https://doi.org/10.1175/MWR-D-13-00204.1.

Jones, T. A., K. Knopfmeier, D. Wheatley, G. Creager, P. Minnis, and R. Palikondo, 2016: Storm-scale data assimilation and ensemble forecasting with the NSSL experimental Warn-on-Forecast system. Part II: Combined radar and satellite data experiments. *Wea. Forecasting*, **31**, 297–327, https://doi.org/10.1175/WAF-D-15-0107.1.

Kain, J. S., S. J. Weiss, J. J. Levit, M. E. Baldwin, and D. R. Bright, 2006: Examination of convective allowing configurations of the WRF Model for the prediction of severe convective weather: The SPC/NSSL spring program 2004. *Wea. Forecasting*, **21**, 167–181, https://doi.org/10.1175/WAF906.1.

——, and Coauthors, 2008: Some practical considerations for the first generation of operational convection allowing NWP: How much resolution is enough? *Wea. Forecasting*, **23**, 931–952, https://doi.org/10.1175/WAF2007106.1.

Keil, C., F. Heinlein, and G. Craig, 2014: The convective adjustment time-scale as indicator of predictability of convective precipitation. *Quart. J. Roy. Meteor. Soc.*, **140**, 480–490, https://doi.org/10.1002/qj.2143.

Kerr, C. A., D. J. Stensrud, and X. Wang, 2017: Verification of convection-allowing model ensemble analyses of near-storm environments using MPEX upsonde observations. *Mon. Wea. Rev.*, **145**, 857–875, https://doi.org/10.1175/MWR-D-16-0287.1.

Leoncini, G., R. Plant, S. Gray, and P. Clark, 2010: Perturbation growth at the convective scale for CSIP IOP18. *Quart. J. Roy. Meteor. Soc.*, **136**, 653–670, https://doi.org/10.1002/qj.587.

Maddox, R. A., 1980: Mesoscale convective complexes. *Bull. Amer. Meteor. Soc.*, **61**, 1374–1387, https://doi.org/10.1175/1520-0477(1980)061<1374:MCC>2.0.CO;2.

Majcen, M., P. Markowski, Y. Richardson, D. Dowell, and J. Wurman, 2008: Multipass objective analyses of Doppler radar data. *J. Atmos. Oceanic Technol.*, **25**, 1845–1858, https://doi.org/10.1175/2008JTECHA1089.1.

Morrison, H., 2016a: Impacts of updraft size and dimensionality on the perturbation pressure and vertical velocity in cumulus convection. Part I: Simple, generalized analytic solutions. *J. Atmos. Sci.*, **73**, 1441–1454, https://doi.org/10.1175/JAS-D-15-0040.1.

——, 2016b: Impacts of updraft size and dimensionality on the perturbation pressure and vertical velocity in cumulus convection. Part II: Comparison of theoretical and numerical solutions and fully dynamical simulations. *J. Atmos. Sci.*, **73**, 1455–1480, https://doi.org/10.1175/JAS-D-15-0041.1.

Parker, M. D., 2014: Composite VORTEX2 supercell environments from near-storm soundings. *Mon. Wea. Rev.*, **142**, 508–529, https://doi.org/10.1175/MWR-D-13-00167.1.

Romine, G. S., C. S. Schwartz, R. D. Torn, and M. L. Weisman, 2016: Impact of assimilating dropsonde observations from MPEX on ensemble forecasts of severe weather events. *Mon. Wea. Rev.*, **144**, 3799–3823, https://doi.org/10.1175/MWR-D-15-0407.1.

Skamarock, W. C., and Coauthors, 2008: A description of the Advanced Research WRF version 3. NCAR Tech. Note NCAR/TN-475+STR, 113 pp., https://doi.org/10.5065/D68S4MVH.

Sobash, R. A., and D. J. Stensrud, 2015: Assimilating surface mesonet observations with the EnKF to improve ensemble forecasts of convection initiation on 29 May 2012. *Mon. Wea. Rev.*, **143**, 3700–3725, https://doi.org/10.1175/MWR-D-14-00126.1.

——, and L. J. Wicker, 2015: On the impact of additive noise in storm-scale EnKF experiments. *Mon. Wea. Rev.*, **143**, 3067–3086, https://doi.org/10.1175/MWR-D-14-00323.1.

——, G. S. Romine, C. S. Schwartz, D. J. Gagne, and M. L. Weisman, 2016: Explicit forecasts of low-level rotation from convection-allowing models for next-day tornado prediction. *Wea. Forecasting*, **31**, 1591–1614, https://doi.org/10.1175/WAF-D-16-0073.1.

Stensrud, D. J., 1996: Effects of a persistent, midlatitude mesoscale region of convection on the large-scale environment during the warm season. *J. Atmos. Sci.*, **53**, 3503–3527, https://doi.org/10.1175/1520-0469(1996)053<3503:EOPMMR>2.0.CO;2.

——, and J. L. Anderson, 2001: Is midlatitude convection an active or a passive player in producing global circulation patterns. *J. Climate*, **14**, 2222–2237, https://doi.org/10.1175/1520-0442(2001)014<2222:IMCAAO>2.0.CO;2.

——, and Coauthors, 2009: Convective-scale Warn-on-Forecast system: A vision for 2020. *Bull. Amer. Meteor. Soc.*, **90**, 1487–1499, https://doi.org/10.1175/2009BAMS2795.1.

——, and Coauthors, 2013: Progress and challenges with Warn-on-Forecast. *Atmos. Res.*, **123**, 2–16, https://doi.org/10.1016/j.atmosres.2012.04.004.

Thompson, G., P. R. Field, R. M. Rasmussen, and W. D. Hall, 2008: Explicit forecasts of winter precipitation using an improved bulk microphysics scheme. Part II: Implementation of a new snow parameterization. *Mon. Wea. Rev.*, **136**, 5095–5115, https://doi.org/10.1175/2008MWR2387.1.

Torn, R. D., and G. J. Hakim, 2008: Ensemble-based sensitivity analysis. *Mon. Wea. Rev.*, **136**, 663–677, https://doi.org/10.1175/2007MWR2132.1.

——, and G. S. Romine, 2015: Sensitivity of central Oklahoma convection forecasts to upstream potential vorticity anomalies during two strongly forced cases during MPEX. *Mon. Wea. Rev.*, **143**, 4064–4087, https://doi.org/10.1175/MWR-D-15-0085.1.

——, ——, and T. J. Galarneau Jr., 2017: Sensitivity of dryline convection forecasts to upstream forecast errors for two weakly forced MPEX cases. *Mon. Wea. Rev.*, **145**, 1831–1852, https://doi.org/10.1175/MWR-D-16-0457.1.

Trapp, R. J., D. J. Stensrud, M. C. Coniglio, R. S. Schumacher, M. E. Baldwin, S. Waugh, and D. T. Conlee, 2016: Mobile radiosonde deployments during the Mesoscale Predictability Experiment (MPEX): Rapid and adaptive sampling of upscale convective feedbacks. *Bull. Amer. Meteor. Soc.*, **97**, 329–336, https://doi.org/10.1175/BAMS-D-14-00258.1.

Wagner, T. J., W. F. Feltz, and S. A. Ackerman, 2008: The temporal evolution of convective indices in storm-producing environments. *Wea. Forecasting*, **23**, 786–794, https://doi.org/10.1175/2008WAF2007046.1.

Weisman, M. L., and Coauthors, 2015: The Mesoscale Predictability Experiment (MPEX). *Bull. Amer. Meteor. Soc.*, **96**, 2127–2149, https://doi.org/10.1175/BAMS-D-13-00281.1.

Wheatley, D. M., D. J. Stensrud, D. C. Dowell, and N. Yussouf, 2012: Application of a WRF mesoscale data assimilation system to springtime severe weather events 2007–09. *Mon. Wea. Rev.*, **140**, 1539–1557, https://doi.org/10.1175/MWR-D-11-00106.1.

——, N. Yussouf, and D. J. Stensrud, 2014: Ensemble Kalman filter analyses and forecasts of a severe mesoscale convective system using different choices of microphysics schemes. *Mon. Wea. Rev.*, **142**, 3243–3263, https://doi.org/10.1175/MWR-D-13-00260.1.

——, K. H. Knopfmeier, T. A. Jones, and G. J. Creager, 2015: Storm-scale data assimilation and ensemble forecasting with the NSSL Experimental Warn-on-Forecast System. Part I: Radar data experiments. *Wea. Forecasting*, **30**, 1795–1817, https://doi.org/10.1175/WAF-D-15-0043.1.

Wilks, D. S., 2011: *Statistical Methods in the Atmospheric Sciences.* Academic Press, 676 pp.

Yussouf, N., E. R. Mansell, L. J. Wicker, D. M. Wheatley, and D. J. Stensrud, 2013: The ensemble Kalman filter analyses and forecasts of the 8 May 2003 Oklahoma City tornadic supercell storm using single- and double-moment microphysics schemes. *Mon. Wea. Rev.*, **141**, 3388–3412, https://doi.org/10.1175/MWR-D-12-00237.1.

Zhang, F., N. Bei, R. Rotunno, C. Snyder, and C. C. Epifanio, 2007: Mesoscale predictability of moist baroclinic waves: Convection-permitting experiments and multistage error growth dynamics. *J. Atmos. Sci.*, **64**, 3579–3594, https://doi.org/10.1175/JAS4028.1.